Therapeutics, Targets, and Chemical Biology

Cancer Research

ATM Deficiency Is Associated with Sensitivity to PARP1- and ATR Inhibitors in Lung Adenocarcinoma

Anna Schmitt[1,2], Gero Knittel[1,2], Daniela Welcker[1,2], Tsun-Po Yang[3,4], Julie George[3], Michael Nowak[5], Uschi Leeser[1,2], Reinhard Büttner[6], Sven Perner[7], Martin Peifer[3,4], and Hans Christian Reinhardt[1,2,4]

Abstract

Defects in maintaining genome integrity are a hallmark of cancer. The DNA damage response kinase ATM is frequently mutated in human cancer, but the significance of these events to chemotherapeutic efficacy has not been examined deeply in whole organism models. Here we demonstrate that bi-allelic *Atm* deletion in mouse models of *Kras*-mutant lung adenocarcinoma does not affect cisplatin responses. In marked contrast, *Atm*-deficient tumors displayed an enhanced response to the topoisomerase-II poison etoposide. Moreover, *Atm*-deficient cells and tumors were sensitive to the PARP inhibitor olaparib. This actionable molecular addiction to functional PARP1 signaling was preserved in models that were proficient or deficient in p53, resembling standard or high-risk genetic constellations, respectively. *Atm* deficiency also markedly enhanced sensitivity to the ATR inhibitor VE-822. Taken together, our results provide a functional rationale to profile human tumors for disabling *ATM* mutations, particularly given their impact on PARP1 and ATR inhibitors. *Cancer Res; 77(11); 3040–56. ©2017 AACR.*

Introduction

Lung cancer is the most common cancer entity after nonmelanocytic skin cancer, and lung cancer–related deaths surpass those from any other neoplastic disease worldwide (1). In 2012, lung cancer was the most frequently diagnosed cancer and the leading cause of cancer-related death in male populations. In female patients, lung cancer was the leading cause of cancer-related death in the developed countries, and the second leading cause of cancer-related death in developing countries (2). Through recent cancer genome sequencing efforts, we are beginning to understand the complex genomic aberrations that lead to the development of lung cancer (3). Particularly in lung adenocarcinoma, these efforts have led to the identification of numerous actionable genetic vulnerabilities, such as oncogenic *EGFR* mutations, as well as *ALK* and *ROS1* rearrangements (4). However, the majority of lung adenocarcinomas appear to be driven by oncogenic alterations that are not amenable to direct therapeutic intervention (5). The most prominent example in this regard is oncogenically mutated *KRAS*, which occurs in approximately 32% of lung adenocarcinomas and for which no direct targeting approaches have been clinically developed, thus far (5). While *KRAS* is clearly a potent oncogenic driver, additional genomic aberrations may exist in *KRAS*-driven lung adenocarcinomas that could impact the therapeutic response. For instance, *KRAS* mutations were recently shown to cocluster with mutations affecting the p53 response in lung adenocarcinoma (6). These data suggest that an impaired DNA damage response maybe selected in *KRAS*-mutant lung adenocarcinoma. In line with this observation, it was recently shown that approximately 40% of human lung adenocarcinomas lack ATM protein expression (7).

The DNA damage response (DDR) constitutes a complex, kinase-based signaling network, which is activated in response to genotoxic stress (8). The DDR consists of two major branches, namely the ATR/CHK1 and the ATM/CHK2 pathways, in which the proximal kinases ATR and ATM directly phosphorylate and activate the effector kinases CHK1 and CHK2, respectively (8). Beyond these canonical kinase branches, additional signaling components, such as the p38MAPK/MK2 pathway, are recruited into the DDR network, depending on the type of genotoxic stress (9–12). The proximal DDR kinase ATM is a master regulator of the DDR and is involved in mediating cell-cycle arrest, DNA repair and apoptosis, following DNA damage (13–15). In keeping with the prominent role of ATM in cell cycle control, DNA repair, and genome maintenance, the *ATM* gene is recurrently inactivated through mutations and/or deletions in various cancer entities, ranging from hematologic malignancies to solid tumors,

[1]Department I of Internal Medicine, University Hospital of Cologne, Cologne, Germany. [2]Cologne Excellence Cluster on Cellular Stress Response in Aging-Associated Diseases, University of Cologne, Cologne, Germany. [3]Department of Translational Genomics, Center of Integrated Oncology Cologne-Bonn, Medical Faculty, University of Cologne, Cologne, Germany. [4]Center for Molecular Medicine Cologne (CMMC), University of Cologne, Cologne, Germany. [5]Institute of Pathology, University Hospital Bonn, Bonn, Germany. [6]Institute of Pathology, University Hospital of Cologne, Cologne, Germany. [7]Department of Pathology, University Medical Center Schleswig-Holstein, Campus Luebeck and the Research Center Borstel, Leibniz Center for Medicine and Biosciences, Luebeck and Borstel, Germany.

Note: Supplementary data for this article are available at Cancer Research Online (http://cancerres.aacrjournals.org/).

Corresponding Authors: Hans Christian Reinhardt, Department I of Internal Medicine, University Hospital of Cologne, Weyertal 115B, Cologne 50931, Germany. Phone: 4922-1478-96701; Fax: 4922-1478-96719; E-mail: christian.reinhardt@uk-koeln.de; and Anna Schmitt, anna.schmitt@uk-koeln.de.

doi: 10.1158/0008-5472.CAN-16-3398

including lung adenocarcinoma (3, 5, 16–19). Specifically in chronic lymphocytic leukemia, it was shown that biallelic loss of *ATM* is associated with poor prognosis of the affected patients (20). This may be rationalized by the observation that *ATM* depletion impairs chemotherapy-induced p53 activation and subsequent induction of p53-dependent apoptosis (21). Beyond its role in regulating p53-mediated apoptosis, ATM is also involved in DNA double-strand break (DSB) repair, particularly through the homologous recombination (HR) pathway, with a less well defined role in the nonhomologous end joining pathway (15). ATM was specifically shown to mediate DSB resection and subsequent recruitment of the critical HR component RAD51 to the sites of damage (15). Recent reports further suggest that ATM is particularly involved in mediating DSB repair in heterochromatin regions of the genome through a slow-acting repair process (22, 23). It was shown that ATM directly phosphorylates the heterochromatin-building factor KAP-1, which in turn promotes HR-mediated DSB repair within heterochromatin regions (22, 23). In line with these observations, KAP-1 depletion was demonstrated to rescue the DSB repair defect induced by ATM deficiency (22, 23).

Intriguingly, both preclinical and clinical observations strongly suggest that a defective HR pathway is associated with distinct molecular liabilities. For instance, it was recently shown that *BRCA1*- or *BRCA2*-deficient cells and tumors, which display a manifest HR defect, are extraordinarily sensitive against PARP1 inhibition (24, 25). Furthermore, *in vitro* single-agent ATR inhibition was recently shown to induce selective toxicity in Chinese hamster cells that were HR-defective, due to *ATM*, *BRCA2*, or *XRCC3* alterations, nucleotide excision repair–defective, due to *ERCC2* mutations, or base excision repair–defective, due to *XRCC1* defects (26). Specifically the selective toxicity of ATR inhibition in HR-defective cells is further corroborated by *in vitro* experiments that demonstrated that RAD51 depletion or inhibition led to a massively increased sensitivity against ATR or Chk1 inhibitors (27). However, the *in vivo* efficacy of ATR inhibitors has not been conclusively shown to date.

Here, we employ autochthonous mouse models of *Kras*-driven lung adenocarcinoma, as well as orthotopic transplantation models of genetically engineered lung adenocarcinoma cells in a syngeneic system to assess molecular vulnerabilities associated with *Atm* deficiency in lung adenocarcinoma. Our models span standard risk ($Kras^{G12D}$) to high-risk ($Kras^{G12D};Tp53^{-/-}$) genetic constellations. We show that loss of *Atm* is tolerated in *Tp53*-proficient backgrounds, while it appears to be counterselected in *Tp53*-deficient settings, *in vivo*. We further demonstrate that *Atm* deficiency is associated with markedly increased sensitivity against PARP1 and ATR inhibition, regardless of the *Tp53* status. These data strongly suggest that even in lung adenocarcinomas displaying a high-risk mutational constellation, response to targeted small-molecule drugs is dictated by additional mutations affecting the DDR. Our data further indicate that the *ATM* status should routinely be assessed in lung adenocarcinomas, as defective ATM signaling is associated with an actionable dependence on PARP1 and ATR.

Materials and Methods

Autochthonous murine lung adenocarcinoma model

We employed the $Kras^{LSL.G12D/wt}$ (K) and $Kras^{LSL.G12D/wt};Tp53^{fl/fl}$ (KP) mouse model for *Kras*-driven lung adenocarcinoma, as described previously (28). In addition, we combined a conditional *Atm* allele (Atm^{fl}) (29) with the K and KP models, to obtain $Kras^{LSL.G12D/wt};Atm^{fl/fl}$ (KA) and $Kras^{LSL.G12D/wt};Tp53^{fl/fl};Atm^{fl/fl}$ (KPA) mice, respectively. Mice were kept on a mixed *C57Bl6*/*Sv129* background. To induce lung tumor formation, 8- to 12-week-old mice were anesthetized with Ketavet (100 mg/kg) and Rompun (20 mg/kg) by intraperitoneal injection followed by intratracheal instillation of replication-deficient adenovirus expressing Cre-recombinase (Adeno-Cre, 2.5×10^7 PFU). To confirm tumor formation, KP and KPA mice were scanned five weeks after Adeno-Cre application by μCT imaging (Aloka, Latheta LCT-100) under isoflurane (2.5%) anesthesia. K and KA mice were imaged 12 weeks after tumor induction in the same manner. All mouse experiments were conducted in accordance with an Institutional Animal Care and Use Committee (IACUC).

Allograft model

For the syngeneic allograft experiment, mice were anesthetized (2.5% isoflurane) and injected with 1.5×10^6 tumor cells into the right lung. Tumor formation was verified by μCT imaging one week after injection. Mice were subjected to four different treatment regimens and tumor volume changes were monitored by weekly μCT imaging for four weeks. Tumor volume was assessed by OsiriX and DICOM viewer software packages (OsiriX v.8.2, Pixmeo).

Compound solutions were prepared as follows: the PARP inhibitor olaparib (Axon Medchem, AZD2281) was dissolved in dimethyl sulfoxide to a final concentration of 50 mg/mL and then added to 10% 2-hydroxy-propyl-beta-cyclodextrin/PBS solution. Olaparib was administered daily at a dose of 50 mg/kg i.p. The ATR inhibitor VE-822 (Abmole, M3115) was dissolved in an equilibrated (v/v) mixture PBS (70%), polyethylene glycol 300 (PEG300, 29.5%) and Tween 80 (0.5%) at a concentration of 18 mg/mL. VE-822 was administered weekly for 3 consecutive days at a dose of 30 mg/kg by oral gavage. Etoposide (Hexal) was administered two times for 4 consecutive days, intraperitoneally, at a concentration of 10 mg/kg. Cisplatin (Accord) was administered once a week for 3 consecutive weeks at a concentration of 7.5 mg/kg, i.p.

Histologic analysis and tumor volume quantification

Mice harboring tumors of all four genoytpes were sacrificed 4, 8, and 12 weeks after Adeno-Cre inhalation and lungs were fixed in 4% PFA. Formalin-fixed paraffin-embedded (FFPE) murine lung samples were cut into 4 μm–thick sections and mounted on slides. After staining with haematoxylin and eosin (H&E), the tumors were assessed by a board-certified pathologist to evaluate the relative tumor burden. A tumor grading system with two tumor grades (I and II) based on the relative amount of diffuse or nodular tumor growth was applied, exactly as described previously (30). Grade I ("diffuse") tumors were defined by a predominantly diffuse tumor architecture (>90% diffuse). Grade II ("nodular") tumors predominantly show a nodular growth pattern (>90% nodular). In addition, FFPE lungs were stained for the proliferation marker Ki-67 (Cell Signaling Technology, #9661).

Tumor isolation and cell culture

Individual murine lung adenocarcinoma tumor nodules from KP and KPA mice were isolated and cultured in RPMI medium containing 10% FBS and 1% penicillin/streptomycin. The retained *LoxP*-flanked *Atm* allele in $KPA^{fl/\Delta}$ cells was recombined

by treatment with 2.5×10^7 PFU of Adeno-Cre and individual *Atm*-deficient clones ($KPA^{\Delta/\Delta}$) were generated by clone picking.

Results

KRAS-mutant lung adenocarcinomas with cooccurring *TP53* mutations constitute a high-risk collective

KRAS is one of the most frequently mutated oncogenes in human cancer and is altered in 32% of human lung adenocarcinomas. *KRAS*-mutant lung adenocarcinomas remain a clinically challenging subentity, as no effective targeted single-agent or combination regimens are available in the clinical setting. In fact, current first-line regimens for the treatment of stage IV *KRAS*-mutant lung adenocarcinomas consist of platinum-based combination chemotherapy together with a VEGF-blocking antibody (4). Only very recently, immune checkpoint–blocking antibodies are entering the first-line setting in selected patient populations. To approach these difficult to treat *KRAS*-mutant tumors, we initially analyzed publicly available cancer genome sequencing data to ask whether we could identify cooccurring genetic aberrations (7). Consistent with previously published data (3), we found that protein-damaging *TP53* mutations, *MDM2* amplifications, and *CDKN2A* alterations are frequently detected in *KRAS*-mutant lung adenocarcinomas (Fig. 1A). Moreover, patients with *KRAS* mutations and cooccurring alterations in *TP53*, *MDM2*, or *CDKN2A* displayed a reduced overall survival, compared with patients carrying *KRAS*-mutant tumors, in which the integrity of *TP53*, *MDM2*, or *CDKN2A* was preserved (Fig. 1B). These data are mimicked in a well-established murine model of *Kras*-driven lung adenocarcinoma. In these mice, expression of oncogenic $Kras^{G12D}$

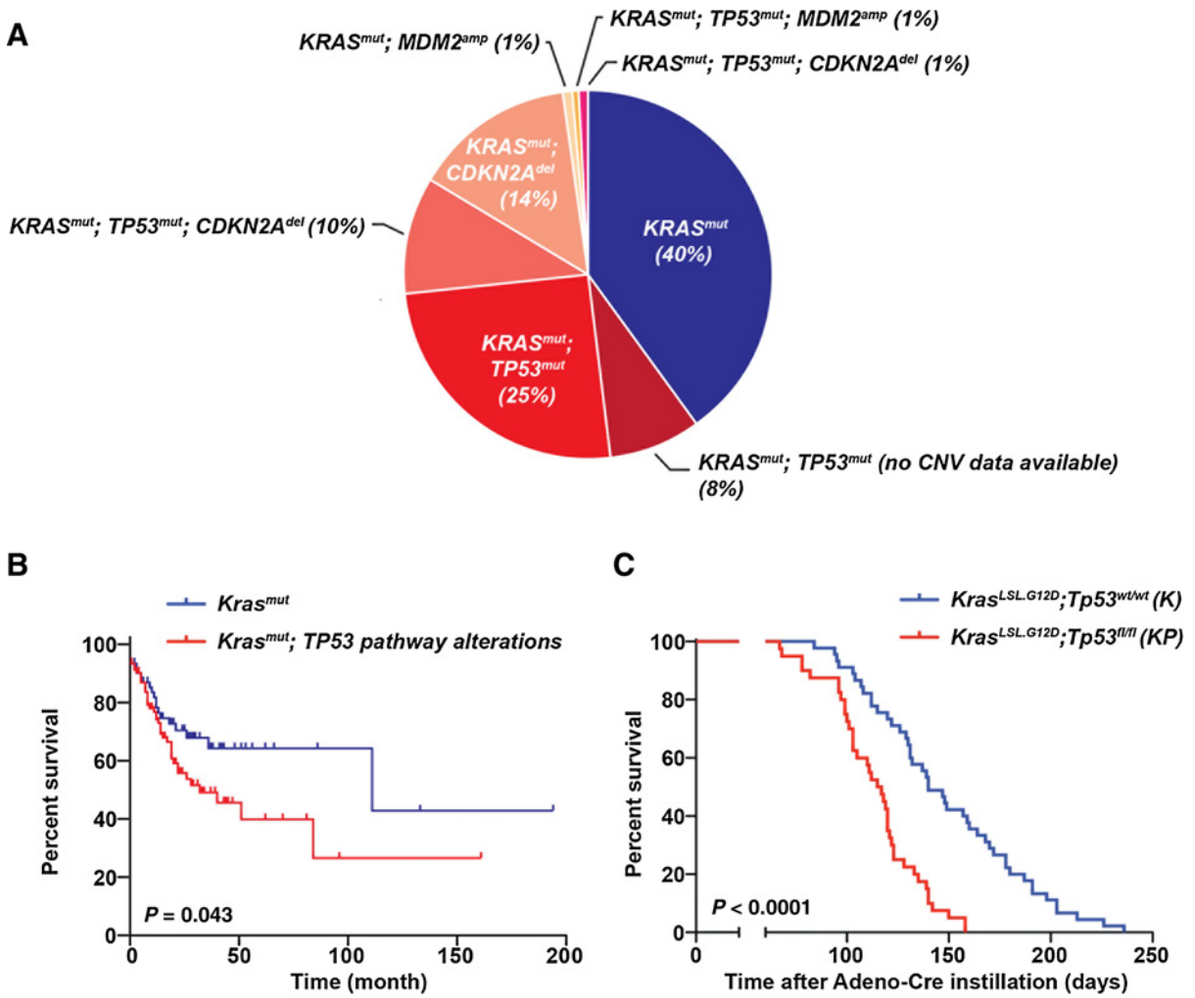

Figure 1.

Combined genomic alterations in *KRAS* and the *TP53* pathway are associated with adverse risk in lung adenocarcinoma patients. **A,** Pie chart based on 146 patients analyzed for the occurrence of mutations in *KRAS* and/or the *TP53* pathway. *TP53* mutations, *MDM2* amplifications, or *CDKN2A* deletions were considered as p53 pathway mutations for this analysis. **B,** Lung adenocarcinomas with combined mutations in *KRAS* and the *TP53* signaling pathway are associated with poor prognosis. Survival of patients that with *KRAS* mutations ($n = 58$), but lacking *TP53* pathway mutations, was compared to the survival of patients with *KRAS* mutations and *TP53* pathway mutations ($n = 88$) by log-rank (Mantel–Cox) test. **C,** $Kras^{LSL.G12D/wt}$;$Tp53^{fl/fl}$ (*KP*) animals ($n = 40$) succumb to their disease significantly earlier than $Kras^{LSL.G12D/wt}$ (*K*) animals ($n = 44$). Mice from both cohorts were subjected to intratracheal instillation of Adeno-Cre with 8–12 weeks of age. Survival of the two groups was compared by log-rank (Mantel–Cox) test.

is prevented through the insertion of a *LoxP*-flanked transcriptional and translational STOP cassette in the endogenous locus ($Kras^{LSL.G12D}$ allele; refs. 6, 28). Intratracheal administration of adenoviral Cre recombinase (Adeno-Cre) leads to the expression of oncogenic $Kras^{G12D}$ from its endogenous locus. In addition to this simple *Kras*-driven model, we also used $Kras^{LSL.G12D/wt}$;$Tp53^{fl/fl}$ mice, in which both *Tp53* alleles are flanked by *LoxP* sites (6, 28, 31). In these compound-mutant mice, Adeno-Cre drives expression of $Kras^{G12D}$ and simultaneous deletion of both *Tp53* alleles. As shown in Fig. 1C, and consistent with previously published data (28), biallelic deletion of *Tp53* in *Kras*-driven lung adenocarcinomas leads to a significantly reduced overall survival, compared with p53-proficient settings.

A recent report indicates that *ATM* is inactivated in approximately 40% of human lung adenocarcinomas (7). Furthermore, it was recently shown that, albeit rarely, inactivation of *ATM* can also occur in *TP53*-deficient human tumors (21). This observation is somewhat surprising, as the proximal DNA damage response kinase ATM directly phosphorylates and activates p53 in a linear pathway. Thus, these observations suggest that cancer cells might derive additional benefit from inactivating the ATM/p53 pathway both, on the level of ATM and p53. Given that ATM is a master regulator of the cellular DNA damage response that is not only involved in activating p53, but also regulates DNA repair and kinase-driven cell-cycle checkpoint networks, we speculated that *KRAS*-driven lung adenocarcinomas with combined *ATM* and *TP53* mutations might display actionable molecular liabilities, despite the fact that simultaneous *KRAS*- and *TP53* alterations constitute a high-risk scenario, *per se*.

Atm alterations lead to reduced overall survival in an autochthonous $Kras^{LSL.G12D/wt}$;$Tp53^{fl/fl}$ mouse model of lung adenocarcinoma

To directly investigate the phenotype associated with *Atm* deficiency in *Kras*-driven tumors *in vivo*, we employed a conditional *LoxP*-flanked *Atm* allele (29), which was homozygously crossed into our $Kras^{LSL.G12D/wt}$ and $Kras^{LSL.G12D/wt}$;$Tp53^{fl/fl}$ models, yielding $Kras^{LSL.G12D/wt}$;$Atm^{fl/fl}$ and $Kras^{LSL.G12D/wt}$;$Tp53^{fl/fl}$;$Atm^{fl/fl}$ mice, respectively (Fig. 2A; Supplementary Fig. S1A).

The biological effects of *Atm* deletion were primarily assessed through recording of overall survival of $Kras^{LSL.G12D/wt}$, $Kras^{LSL.G12D/wt}$;$Tp53^{fl/fl}$, $Kras^{LSL.G12D/wt}$;$Atm^{fl/fl}$ and $Kras^{LSL.G12D/wt}$;$Tp53^{fl/fl}$;$Atm^{fl/fl}$ mice that were intratracheally instilled with Adeno-Cre (2.5×10^7 PFU) at 8–12 weeks of age. As shown in Supplementary Fig. S1A, the survival of $Kras^{LSL.G12D/wt}$ ($n = 17$) and $Kras^{LSL.G12D/wt}$;$Atm^{fl/fl}$ animals ($n = 9$) was not statistically different ($P = 0.1596$). Furthermore, neither the number of individual tumor nodules per lung, nor the relative tumor volume, related to normal lung volume, differed significantly between $Kras^{LSL.G12D/wt}$ and $Kras^{LSL.G12D/wt}$;$Atm^{fl/fl}$ animals at 4, 8, and 12 weeks after Adeno-Cre–mediated recombination (Supplementary Fig. S1C and S1D). Of note, efficient deletion of *Atm* was verified in this model, using a RNA *in situ* hybridization approach (Supplementary Fig. S1B). We specifically chose RNA *in situ* hybridization for the assessment of *Atm* deletion, as no specific antibody against murine *Atm* is available for IHC.

In marked contrast, $Kras^{LSL.G12D/wt}$;$Tp53^{fl/fl}$;$Atm^{fl/fl}$ animals ($n = 16$) displayed a significantly ($P < 0.0001$) reduced overall survival, compared with their *Atm*-proficient $Kras^{LSL.G12D/wt}$;$Tp53^{fl/fl}$ counterparts ($n = 20$; Fig. 2B). Moreover, histologic examination of lungs isolated from $Kras^{LSL.G12D/wt}$;$Tp53^{fl/fl}$;$Atm^{fl/fl}$ animals isolated 8 weeks after intratracheal Adeno-Cre instillation, displayed a significantly ($P < 0.0000001$) larger relative tumor volume per lung, compared with $Kras^{LSL.G12D/wt}$;$Tp53^{fl/fl}$ controls (60% ± 0% vs. 10% ± 0% at 8 weeks; Fig. 2C and D). A similar trend was observed in lungs isolated 4 weeks after Adeno-Cre instillation (7.5% ± 2.5% vs. 5% ± 2.5%). However, this trend failed to reach statistical significance (Fig. 2C and D). We did not observe a substantial difference in tumor grade in $Kras^{LSL.G12D/wt}$;$Tp53^{fl/fl}$;$Atm^{fl/fl}$ animals 12 weeks after intratracheal Adeno-Cre instillation, as might have been expected given the massively reduced overall survival of $Kras^{LSL.G12D/wt}$;$Tp53^{fl/fl}$;$Atm^{fl/fl}$ mice compared with $Kras^{LSL.G12D/wt}$;$Tp53^{fl/fl}$ controls (Fig. 2B). As observed in the *Tp53*-proficient setting (Supplementary Fig. S1E), the number of individual tumor nodules per lung did not significantly ($P = 0.1723$) differ between $Kras^{LSL.G12D/wt}$;$Tp53^{fl/fl}$ and $Kras^{LSL.G12D/wt}$;$Tp53^{fl/fl}$;$Atm^{fl/fl}$ animals (Fig. 2E).

To further dissect these observations and to directly assess the efficacy of *Atm* deletion in tumors, we next performed RNA *in situ* hybridization of lungs isolated from tumor-bearing $Kras^{LSL.G12D/wt}$, $Kras^{LSL.G12D/wt}$;$Tp53^{fl/fl}$, $Kras^{LSL.G12D/wt}$;$Atm^{fl/fl}$ and $Kras^{LSL.G12D/wt}$;$Tp53^{fl/fl}$;$Atm^{fl/fl}$ mice 12 weeks after Adeno-Cre application. Surprisingly, we observed incomplete *Atm* deletion in $Kras^{LSL.G12D/wt}$;$Tp53^{fl/fl}$;$Atm^{fl/fl}$ animals (Fig. 2F; Supplementary Fig. S1B). Of note, lungs isolated from $Atm^{-/-}$ mice (32) stained entirely negative for Atm (Fig. 2F, right). Together, these data from $Kras^{LSL.G12D/wt}$, $Kras^{LSL.G12D/wt}$;$Tp53^{fl/fl}$, $Kras^{LSL.G12D/wt}$;$Atm^{fl/fl}$ and $Kras^{LSL.G12D/wt}$;$Tp53^{fl/fl}$;$Atm^{fl/fl}$ mice suggest that biallelic *Atm* deletion is selected against in p53-deficient settings, while it is tolerated in the context of a functional p53 response. Furthermore, the significantly reduced overall survival observed in $Kras^{LSL.G12D/wt}$;$Tp53^{fl/fl}$;$Atm^{fl/fl}$ mice, compared with $Kras^{LSL.G12D/wt}$;$Tp53^{fl/f}$ animals (Fig. 2B) suggests that partial deletion of *Atm* in a *Tp53*-deficient background might enhance tumorigenesis.

Homozygous *Atm* deletions can be obtained in *Tp53*-deficient cells *in vitro*

As combined homozygous deletions of both *Tp53* and *Atm* could not routinely be obtained in $Kras^{G12D}$-driven lung adenocarcinomas *in vivo* (Fig. 2F), we next isolated individual cell lines from tumor-bearing $Kras^{LSL.G12D/wt}$;$Tp53^{fl/fl}$ and $Kras^{LSL.G12D/wt}$;$Tp53^{fl/fl}$;$Atm^{fl/fl}$ animals, to assess their *Tp53* and *Atm* status by genotyping PCR and immunoblot analysis (Fig. 3A–C). We found that $Kras^{LSL.G12D/wt}$;$Tp53^{fl/fl}$- and $Kras^{LSL.G12D/wt}$;$Tp53^{fl/fl}$;$Atm^{fl/fl}$-derived tumor cell lines ($n = 30$ independent clones for each genotype) uniformly displayed a homozygous *Tp53* deletion and a concomitant lack of p53 protein expression (Fig. 3A–C). A different picture emerged, when we analyzed the recombination status of the conditional *Atm* allele in cell lines derived from $Kras^{LSL.G12D/wt}$;$Tp53^{fl/fl}$;$Atm^{fl/fl}$ tumors ($n = 30$ independent clones). Only 1 of 30 independent clones displayed biallelic *Atm* deletion (clone 3; Fig. 3A). Consistent with these genotyping results, ATM protein expression was preserved in 29 of 30 independent clones (only clone c3 lacked ATM protein expression; Fig. 3C and D). Resequencing of the $Kras^{LSL.G12D/wt}$;$Tp53^{fl/fl}$;$Atm^{fl/fl}$–derived tumor cell lines revealed that the *LoxP* sites flanking the nonrecombined *Atm* alleles were intact in all 29 non-recombined clones. These data indicate that acute combined biallelic loss of *Tp53* and *Atm* might be counterselected in *Kras*-driven tumors. Furthermore, the uniform deletion of both *Tp53* alleles might suggest that *Tp53* deficiency provides the incipient *Kras*-mutant cancer cell with traits that are advantageous, compared with

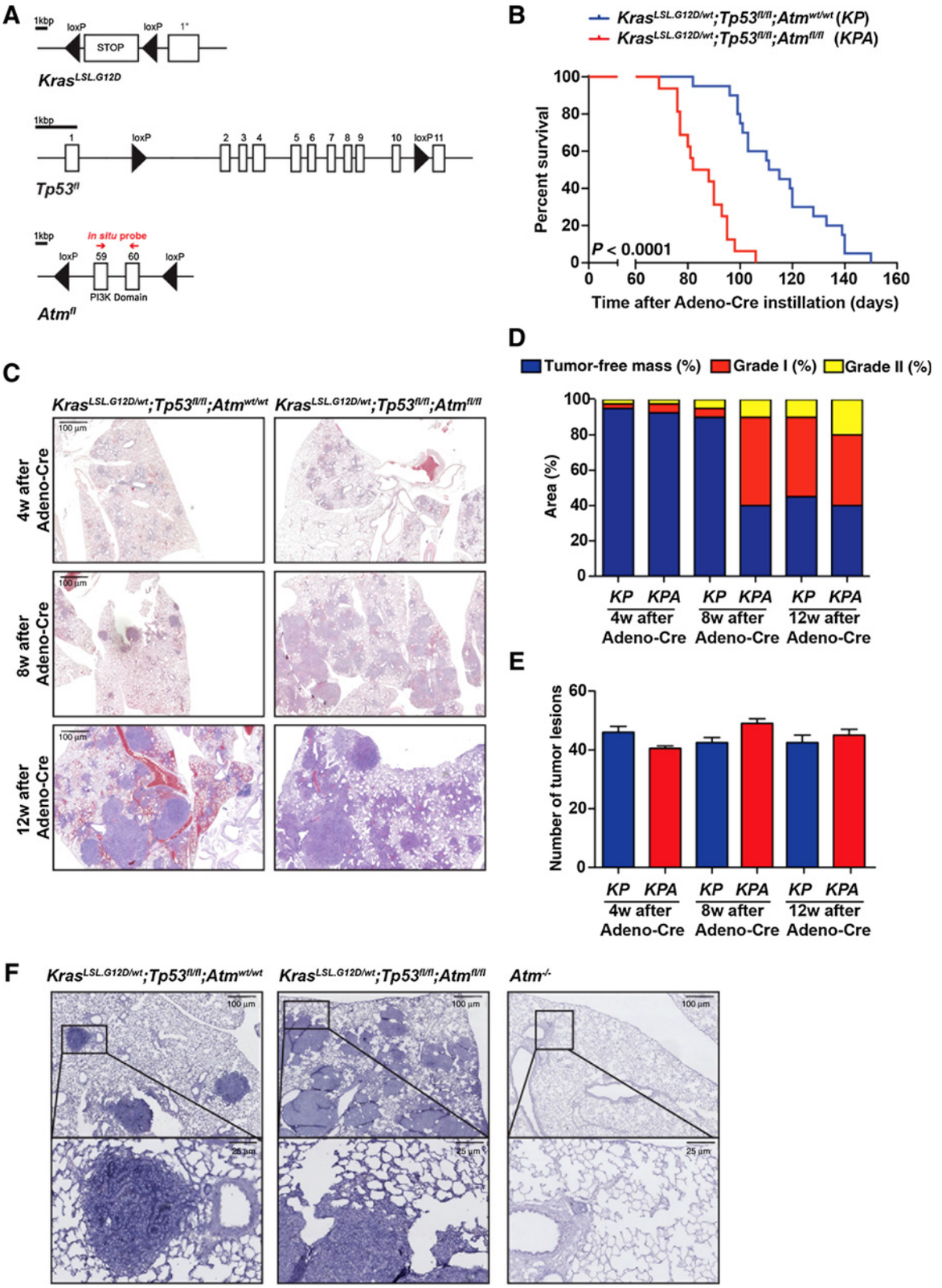

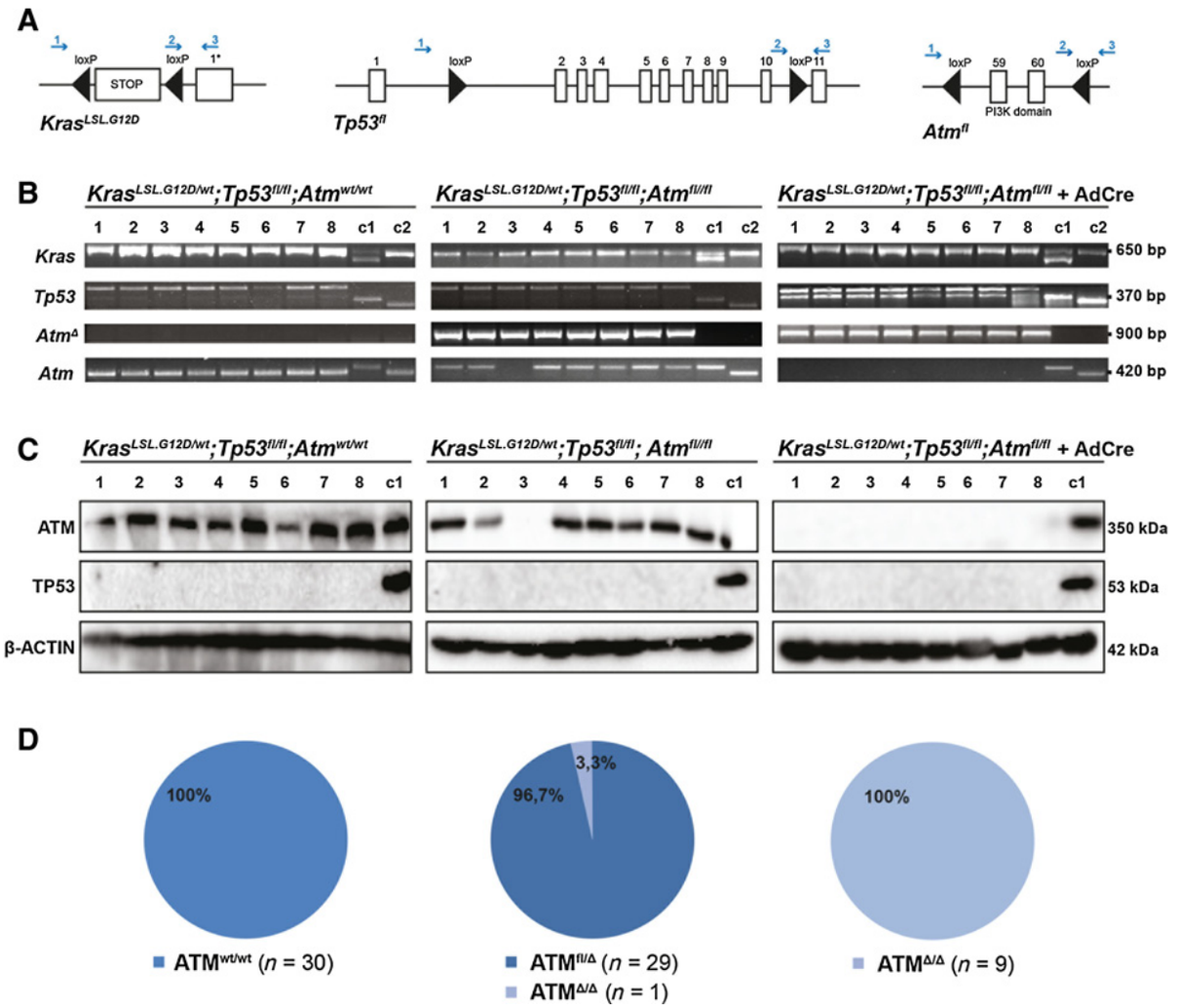

Figure 3.

Deletion of both *Atm* alleles is tolerated in *Kras*$^{LSL.G12D/wt}$; *Tp53*$^{fl/fl}$;*Atm*$^{fl/fl}$ lung adenocarcinoma cells, *in vitro*. **A,** Schematic representation of the targeted alleles and the primer-binding sites. **B** and **C,** *Atm* is heterozygously deleted in the majority of *KPA* cell lines and homozygously deleted following *in vitro* exposure to Adeno-Cre. **B,** *KP* and *KPA* cell lines were genotyped to detect Cre-mediated recombination in the *Kras, Tp53*, and *Atm* loci. All cell lines show efficient recombination of *Kras* (monoallelic) and *Tp53* (biallelic), while only one out of eight *KPA* cell lines showed biallelic *Atm* deletion. Following *in vitro* administration of Adeno-Cre, biallelic *Atm* deletion was readily detected in all *KPA* cell lines. Genotyping was performed by PCR. Displayed bands for *Kras*: wild-type, 622 bp; *LoxP*-flanked allele, 500 bp; recombined allele, 650 bp. Displayed bands for *Tp53*: wild-type, 288 bp: *LoxP*-flanked allele, 370 bp; recombined allele, 612 bp; unspecific band, 400 bp. Displayed bands for *Atm*: wild-type, 328 bp; *LoxP*-flanked allele, 420 bp; recombined allele, 903 bp. c1 = tail DNA from *Kras*$^{LSL.G12D/wt}$; *Tp53*$^{fl/fl}$; *Atm*$^{fl/fl}$ mouse. c2, tail DNA from wild-type mouse. **C,** Immunoblot to detect ATM and TP53 in lysates derived from *KP*-, *KPA*-, and *KPA* cells that were exposed to Adeno-Cre *in vitro*. All cell lines displayed complete loss of TP53 in all samples. ATM was expressed in seven out of eight *KPA* cell lines and was not expressed following *in vitro* administration of Adeno-Cre. β-Actin was used as a loading control. **D,** Schematic representation of the ATM status of all cell lines generated from *KP* ($n = 30$) and *KPA* tumors ($n = 30$) and of *KPA* cell lines, which were treated with Adeno-Cre *in vitro* ($n = 9$).

Figure 2.

Atm alterations in *Tp53*-deficient *Kras*-driven murine lung adenocarcinomas leads to reduced survival and a more aggressive tumor phenotype. **A,** Schematic representation of the three alleles used in the mouse model *Kras*$^{LSL.G12D}$, *Tp53*^{fl}, and *Atm*^{fl}. Two experimental groups were generated, *Kras*$^{LSL.G12D/wt}$;*Tp53*$^{fl/fl}$ (*KP*) and *Kras*$^{LSL.G12D/wt}$;*Tp53*$^{fl/fl}$;*Atm*$^{fl/fl}$ (*KPA*) mice. **B,** *Atm* alterations significantly reduce the overall survival of lung adenocarcinoma-bearing KP mice, *in vivo*. Kaplan–Meier curves illustrate the overall survival of *KP* ($n = 20$) and *KPA* ($n = 16$) mice 160 days following Adeno-Cre application. Log-rank test: $P < 0.0001$. **C,** Representative histology, H&E stainings of lungs isolated from mice 4, 8, and 12 weeks after tumor induction. *KP* and *KPA* mice display progressively growing lung adenocarcinomas following intratracheal Adeno-Cre application. Histologic examination revealed that *KPA* animals display more aggressively growing lung adenocarcinomas than *KP* animals. **D,** Quantification of H&E-stained lung tissue samples indicating tumor-free mass, tumor grade I, and tumor grade II, according to the grading system detailed in Materials and Methods. **E,** No differences in the number of tumor lesions were observed between *KP* and *KPA* mice. Lungs were isolated 4, 8, and 12 weeks after tumor induction ($n = 2$). **F,** *Atm* is still expressed in lungs of *KPA* mice isolated 8 weeks after tumor induction. *Atm in situ* hybridization on lung sections (*KP* and *KPA*) isolated 8 weeks after tumor induction. Tumor-free lungs isolated from an *Atm*$^{-/-}$ mouse were used as a negative control.

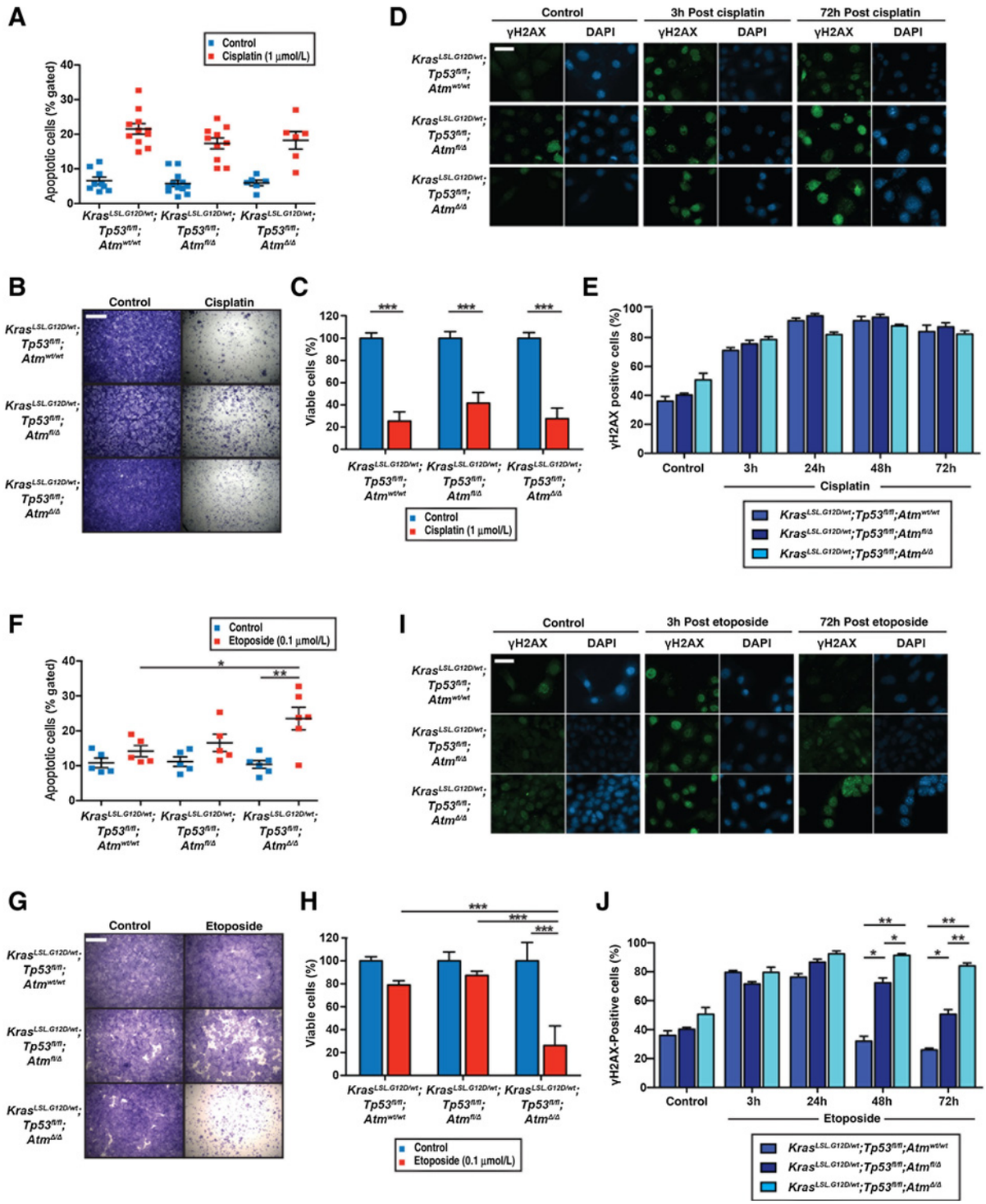

Figure 4.

Atm-defective lung adenocarcinoma cell lines display hypersensitivity to DNA double-strand break-inducing agents. **A,** *KP*-, *KPA*$^{fl/\Delta}$-, *KPA*$^{\Delta/\Delta}$ cell lines display a similar degree of apoptotic cell death in response to cisplatin (1 μmol/L; red). Blue, vehicle-treated cells. Cells were treated for 72 hours and apoptosis was assessed by quantification of the Annexin-V/PI double-positive population using flow cytometry. Average values of three independent experiments are shown. **B** and **C,** *KP*-, *KPA*$^{fl/\Delta}$-, and *KPA*$^{\Delta/\Delta}$ cells show reduced clonogenic survival following cisplatin treatment. **B,** *KP*-, *KPA*$^{fl/\Delta}$-, and *KPA*$^{\Delta/\Delta}$ cell lines were exposed to 1 μmol/L cisplatin or vehicle control for 72 hours. Crystal violet stainings were performed after 10 days in culture. **C,** Quantification of crystal violet–positive cells. Scale bar, 500 μm. **D** and **E,** Cisplatin treatment (10 μm, 30 minutes) induces genotoxic damage *KP*-, *KPA*$^{fl/\Delta}$-, and *KPA*$^{\Delta/\Delta}$ cells. (*Continued on the following page.*)

biallelic *Atm* deficiency. We next asked whether we could achieve biallelic *Atm* deletion in $Kras^{G12D/wt};Tp53^{\Delta/\Delta};Atm^{fl/\Delta}$ cell lines. For this purpose, we reexposed these cell lines to Adeno-Cre (2.5×10^7 PFU/mL of culture media) and assessed the recombination status in individual clones isolated following this *in vitro* Cre-application. As shown in Fig. 3B and C, this *in vitro* Adeno-Cre exposure resulted in efficient deletion of the remaining *LoxP*-flanked *Atm* allele, and subsequent loss of ATM protein expression in all 9 $Kras^{G12D/wt};Tp53^{\Delta/\Delta};Atm^{fl/\Delta}$ parental cell lines. We note that these *in vitro*–derived $Kras^{G12D/wt};Tp53^{\Delta/\Delta};Atm^{\Delta/\Delta}$ clones displayed proliferation kinetics that were not significantly different from those observed in $Kras^{G12D/wt};Tp53^{\Delta/\Delta}$- and $Kras^{G12D/wt};Tp53^{\Delta/\Delta};Atm^{fl/\Delta}$ clones (Supplementary Fig. S2). Thus, in summary, biallelic *Tp53* and *Atm* deletion can be achieved *in vitro*, but appears to be counterselected *in vivo*.

Atm-deficient $Kras^{G12D/wt};Tp53^{\Delta/\Delta}$ lung adenocarcinomas display increased sensitivity against the topoisomerase-II inhibitor etoposide

We next asked whether $Kras^{G12D/wt};Tp53^{\Delta/\Delta}$- (referred to as *KP* hereafter), $Kras^{G12D/wt};Tp53^{\Delta/\Delta};Atm^{fl/\Delta}$- (referred to as $KPA^{fl/\Delta}$ hereafter), and $Kras^{G12D/wt};Tp53^{\Delta/\Delta};Atm^{\Delta/\Delta}$ (referred to as $KPA^{\Delta/\Delta}$ hereafter) cells displayed differential chemotherapy sensitivity *in vitro* (Fig. 4; Supplementary Fig. S3). For this purpose, we employed flow cytometry–based apoptosis measurements and clonogenic colony survival assays. *KP*-, $KPA^{fl/\Delta}$-, and $KPA^{\Delta/\Delta}$ cells were exposed to cisplatin (1 μmol/L), etoposide (0.1 μmol/L), or vehicle control, harvested following 24 hours of drug exposure and subsequently stained, using Annexin V and PI labeling. As shown in Fig. 4A, cisplatin readily induced apoptotic cell death in *KP*-, $KPA^{fl/\Delta}$-, and $KPA^{\Delta/\Delta}$ cells (21.88% ± 0.828%, 17.34% ± 1.57%, and 18.25% ± 2.54%, respectively). However, we did not detect a statistically significant difference in the cisplatin sensitivity of the three different genotypes (Fig. 4A). To validate the results obtained with these flow cytometry experiments, we next performed clonogenic survival assays, using *KP*-, $KPA^{fl/\Delta}$-, and $KPA^{\Delta/\Delta}$ cells. In brief, cells were pretreated with cisplatin (1 μmol/L, 72 hours), trypsinized, and seeded onto new cell culture dishes (5,000 cells per 6-well plate). Fourteen days following seeding, cells were stained with crystal violet and surviving colonies were counted (Fig. 4B and C). Reminiscent of the results obtained in our flow cytometry–based apoptosis measurements, we observed a massive and statistically significant reduction of viable colonies in all three genotypes [$P < 0.0001$ (*KP*), $P < 0.0001$ ($KPA^{fl/\Delta}$) and $P < 0.0001$ ($KPA^{\Delta/\Delta}$); Fig. 4B and C]. However, this reduction in surviving colonies did not differ between *KP*-, $KPA^{fl/\Delta}$-, and $KPA^{\Delta/\Delta}$ cells, further validating our flow cytometry results (Fig. 4B and C). To verify the induction of genotoxic damage induced by cisplatin, we performed a longitudinal assessment of nuclear γH2AX foci, using indirect immunofluorescence (Fig. 4D and E; Supplementary Fig. S3A). These experiments revealed that cisplatin inflicted γH2AX-positive DNA lesions in all three genotypes. The kinetics of DNA damage induction were similar in *KP*-, $KPA^{fl/\Delta}$-, and $KPA^{\Delta/\Delta}$ cells, with a mild induction after 3 hours of drug exposure and a peak at 24 hours. This genotoxic damage remained stable for 72 hours in all three cell types. We did not detect a statistically significant difference in the kinetics and intensity of γH2AX staining between the different genotypes (Fig. 4D and E; Supplementary Fig. S3A).

A strikingly different picture emerged, when we exposed *KP*-, $KPA^{fl/\Delta}$-, and $KPA^{\Delta/\Delta}$ cells to the topoisomerase-II inhibitor etoposide (0.1 μmol/L, 72 hours). Using both flow cytometry–based apoptosis measurements (Fig. 4F), as well as clonogenic survival assays (Fig. 4G), we found that *KP*- and $KPA^{fl/\Delta}$ cells were essentially resistant against etoposide. In marked contrast, etoposide treatment robustly induced substantial levels of apoptosis in $KPA^{\Delta/\Delta}$ cells (Fig. 4F). This difference in apoptosis induction was statistically significant between *KP*- and $KPA^{\Delta/\Delta}$ cells ($P = 0.0385$; Fig. 4F). Similarly, etoposide treatment led to a significant reduction of colony survival only in $KPA^{\Delta/\Delta}$ cells ($P < 0.0001$), but not in *KP*- or $KPA^{fl/\Delta}$ cells (Fig. 4G). Thus, in summary, biallelic *Atm* deletion leads to enhanced etoposide sensitivity in *KP* cells, but does not affect cisplatin sensitivity. We further assessed the severity of genotoxic stress inflicted by etoposide in *KP*-, $KPA^{fl/\Delta}$-, and $KPA^{\Delta/\Delta}$ cells, using immunofluorescence-based longitudinal quantification of nuclear γH2AX foci (Fig. 4I and J; Supplementary Fig. S3B). In all three cell types, we observed a similar peak in genotoxic damage at 24 hours of drug exposure. *KP* cells displayed efficient clearance of γH2AX-positive DNA lesions at 48 and 72 hours following drug treatment. $KPA^{fl/\Delta}$ cells displayed clearance kinetics that were significantly delayed, compared with that observed in *KP* cells. In contrast, $KPA^{\Delta/\Delta}$ cells completely failed to remove γH2AX-positive DNA lesions at 48 and 72 hours. Thus, our cell line panel essentially constitutes an allelic series, where dependent on the *Atm* gene dosage, etoposide-induced DNA damage is repaired (Fig. 4I and J; Supplementary Fig. S3B).

To further substantiate these *in vitro* observations, we next performed orthotopic transplantation experiments to assess chemotherapy sensitivity of *KP*-, $KPA^{fl/\Delta}$-, and $KPA^{\Delta/\Delta}$-derived tumors, *in vivo*. For this purpose, we induced tumors in the lungs of syngeneic-recipient animals through intrathoracal injection of 1.5×10^6 *KP*-, $KPA^{fl/\Delta}$-, or $KPA^{\Delta/\Delta}$ cells, respectively. Tumor onset and therapy response was longitudinally monitored through μCT imaging. Once CT-morphologically visible tumors had formed, animals received either cisplatin (7.5 mg/kg,

(*Continued.*) **D,** Cells were stained with an antibody detecting γH2AX, as well as a DAPI counterstain 3, 24, 48, and 72 hours after treatment. Representative immunofluorescence images are shown. Scale bar, 20 μm. **E,** The percentage of γH2AX positive cells from the experiment detailed in **D** is quantified. **F,** $KPA^{\Delta/\Delta}$ cells display an increased apoptotic response to etoposide treatment (red), compared with *KP*- and $KPA^{fl/\Delta}$ cells. No substantial apoptotic response was observed in the vehicle-treated controls (blue). Cells were treated with 0.1 μmol/L etoposide or vehicle control for 72 hours and the apoptotic fraction was quantified as the Annexin V/PI double-positive population using flow cytometry. Average values of three independent experiments are shown. **G** and **H,** $KPA^{\Delta/\Delta}$ cells display a reduced clonogenic survival after etoposide treatment, compared with *KP*- and $KPA^{fl/\Delta}$ cells. **G,** *KP*-, $KPA^{fl/\Delta}$-, and $KPA^{\Delta/\Delta}$ cell lines were exposed to 0.1 μmol/L etoposide or vehicle control for 72 hours. Crystal violet stainings were performed after 10 days in culture. **H,** Quantification of crystal violet–positive cells. Scale bar, 500 μm. **I** and **J,** Etoposide treatment induces genotoxic damage in *KP*-, $KPA^{fl/\Delta}$-, and $KPA^{\Delta/\Delta}$ cell lines, which is not effectively resolved in $KPA^{\Delta/\Delta}$ cells. **I,** *KP*-, $KPA^{fl/\Delta}$-, and $KPA^{\Delta/\Delta}$ cells were either treated with a vehicle control or with etoposide (10 μmol/L, 30 minutes). Cells were stained for γH2AX and counterstained with DAPI 3, 24, 48, and 72 hours after treatment. Representative immunofluorescence images are shown. Scale bar, 20 μm. **J,** The percentage of γH2AX-positive cells from the experiment detailed in **I** is quantified.

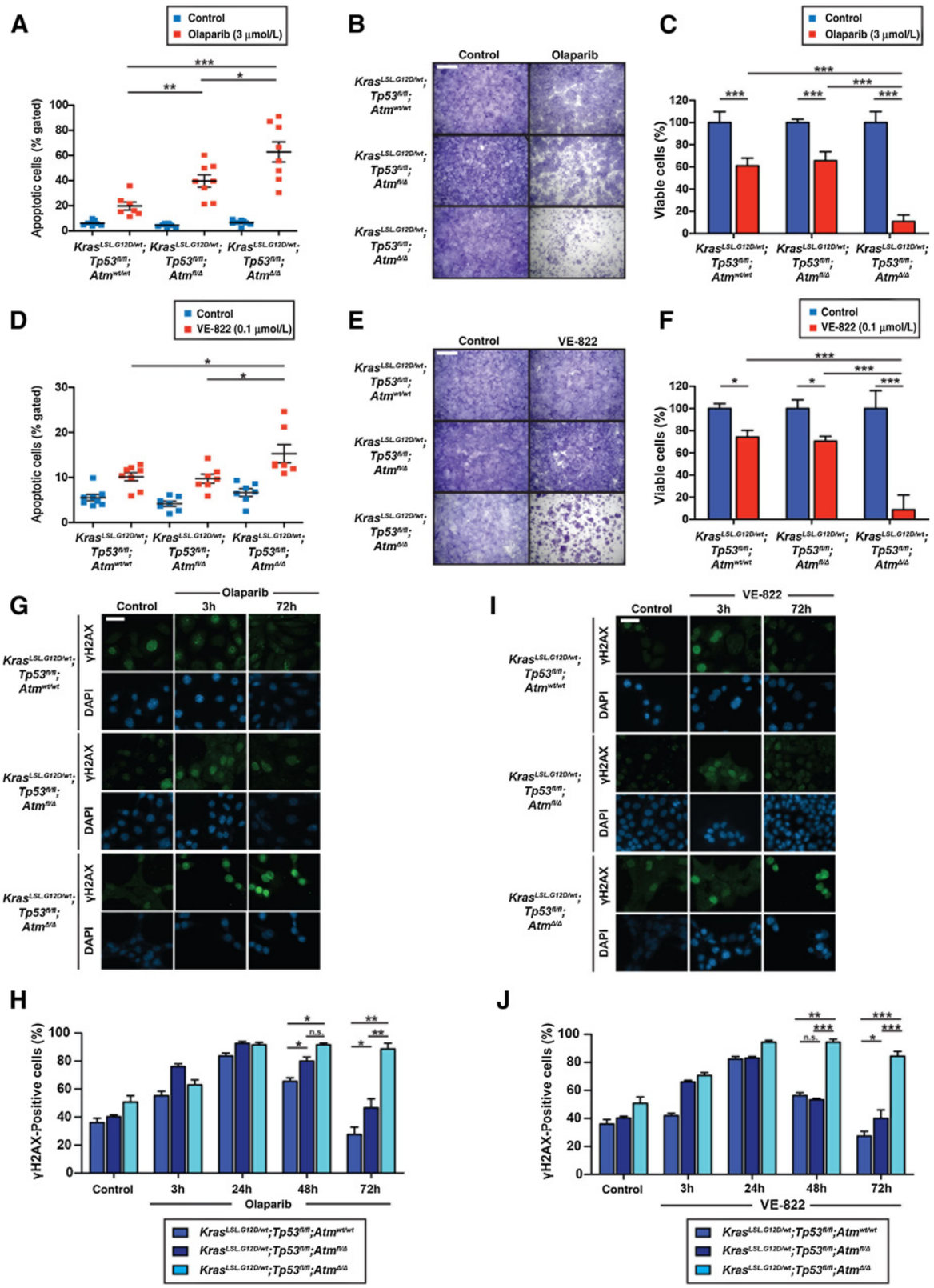

intraperitoneally, days 1, 8, and 15), etoposide (10 mg/kg, intraperitoneally, days 1–5 and 15–19), or vehicle control (Supplementary Fig. S4). As shown in Supplementary Fig. S5A–S5C and corroborating our *in vitro* data, cisplatin treatment led to a reduction in tumor volume, which did not significantly differ between *KP*-, $KPA^{fl/\Delta}$-, and $KPA^{\Delta/\Delta}$-derived tumors. We note that vehicle-treated *KP*-, $KPA^{fl/\Delta}$-, and $KPA^{\Delta/\Delta}$-derived tumors displayed continuous growth throughout the entire observation period of 21 days (Supplementary Fig. S5B and S5C). The cisplatin-induced reduction in tumor volume did not translate into a significant survival gain in any of the three different tumor genotypes, although we detected a trend toward enhanced overall survival in all three genotypes, following cisplatin treatment (Supplementary Fig. S5D). The apparent resistance of the *KP* model against cisplatin-based chemotherapy is in line with observations that we have previously published (30). We next employed IHC to assess the proliferation index (Ki-67–positive tumor cell fraction) in *KP*-, $KPA^{fl/\Delta}$-, and $KPA^{\Delta/\Delta}$-derived tumors, following cisplatin treatment (Supplementary Figs. S5E and S5F and S6). In line with our previous results, we detected a significantly reduced Ki-67 index in all three tumor genotypes, following cisplatin treatment (Supplementary Fig. S5E and S5F and S6). Thus, overall, there appears to be no differential cisplatin sensitivity between *KP*-, $KPA^{fl/\Delta}$-, and $KPA^{\Delta/\Delta}$ cells *in vitro* and tumors *in vivo*.

In contrast to the cisplatin response, our orthotopic transplantation model revealed statistically significant differences in the etoposide response of *KP*-, $KPA^{fl/\Delta}$-, and $KPA^{\Delta/\Delta}$-derived tumors (Supplementary Fig. S7). While *KP*-derived tumors were entirely resistant against etoposide and even displayed mild tumor volume gains (1.476 ± 0.237 fold change in mean tumor volume) one week following application of two cycles of etoposide (10 mg/kg, intraperitoneally, days 1–5 and 15–19), $KPA^{fl/\Delta}$-derived tumors shrank in response to etoposide (0.876 ± 0.032 fold change in mean tumor volume). However, this effect did not reach statistical significance ($P = 0.1272$) at day 7 (Supplementary Fig. S7C) and only reached significance at the day 14 and 21 μCT scans (Supplementary Fig. S7B). In contrast to *KP*- and $KPA^{fl/\Delta}$-derived tumors, $KPA^{\Delta/\Delta}$ tumors displayed a robust and significant ($P = 0.0053$) shrinkage following etoposide treatment (0.620 ± 0.103 fold change in mean tumor volume). This difference was manifest on day 7 (Supplementary Fig. S7C), following the first etoposide dose and remained stable on days 14 and 21 following etoposide (Supplementary Fig. S7B). We note that vehicle-treated *KP*-, $KPA^{fl/\Delta}$-, and $KPA^{\Delta/\Delta}$-derived tumors displayed continuous growth throughout the entire observation period of 21 days (Supplementary Fig. S7B). In line with these CT-morphologic tumor volume–based response data, we also observed a significantly enhanced overall survival of $KPA^{fl/\Delta}$- and $KPA^{\Delta/\Delta}$- tumor-bearing mice, compared with *KP* tumor–bearing animals in response to two cycles of etoposide treatment (Supplementary Fig. S7D). The CT-morphologic response data, as well as the overall survival data, are also reflected by results obtained from IHC analysis of tumor sections from animals that were sacrificed after the first cycle of etoposide treatment (Supplementary Figs. S7E and S7F and S6). While *KP*-derived tumors showed only a mild reduction in Ki-67 positivity following etoposide, $KPA^{fl/\Delta}$- and, even more pronounced, $KPA^{\Delta/\Delta}$-derived tumors displayed a massive reduction in Ki-67 positivity (Supplementary Figs. S7E and S7F and S6). Overall, these data suggest that heterozygous and particularly homozygous *Atm* deletion in *KP*-derived tumors is associated with a significantly enhanced etoposide response. These data indicate that the clinical annotation of the *ATM* status might be a useful tool to predict the etoposide response in high-risk $KRAS^{mut}$ and $TP53^{mut}$ human tumors.

Atm-deficient $Kras^{G12D/wt}$;$Tp53^{fl/fl}$ lung adenocarcinoma cells display actionable molecular dependencies on PARP1 and ATR

ATM is a master regulator of the cellular DNA damage response, which phosphorylates a variety of proteins involved in cell-cycle arrest, DNA repair, and programmed cell death (8, 13, 14). Particularly the role of ATM in DNA DSB repair might be therapeutically relevant: human and murine cells employ two dominant pathways for DSB repair, namely HR, which partially depends on ATM (15) and nonhomologous end joining (15, 33–35). One of the first steps of HR-mediated DSB repair is the resection of the DSB leading to the generation of a single-stranded (ss) 3′-overhang, which is immediately coated by the single-strand–binding protein RPA (15, 36–39). RPA is ultimately

Figure 5.

Combined loss of *Atm* and *Tp53* in *Kras*-driven lung adenocarcinoma cell lines constitutes a genetic constellation that is associated with sensitivity to ATR and PARP inhibition. **A,** Olaparib induces apoptosis in $KPA^{fl/\Delta}$ cells, which was even more pronounced in $KPA^{\Delta/\Delta}$ cells. In contrast, olaparib did not induce a substantial degree of apoptosis in *KP* cells. Cells were treated with 3 μmol/L olaparib (red) or vehicle control (blue) for 120 hours and the apoptotic fraction was quantified as the Annexin V/PI double-positive population using flow cytometry. Average values of three independent experiments are shown. **B** and **C,** Olaparib induces a mild reduction in clonogenic survival of *KP* cells. This effect was enhanced in $KPA^{fl/\Delta}$ cells and even more striking in $KPA^{\Delta/\Delta}$ cells. **B,** *KP*-, $KPA^{fl/\Delta}$-, and $KPA^{\Delta/\Delta}$ cell lines were exposed to 3 μmol/L olaparib or vehicle control for 120 hours. Crystal violet stainings were performed after 10 days in culture. **C,** Quantification of crystal violet–positive cells. Scale bar, 500 μm. **D,** $KPA^{\Delta/\Delta}$ cells display an increased apoptotic response to VE-822 treatment (red), while *KP*- and $KPA^{fl/\Delta}$ cells do not induce substantial apoptosis in response to VE-822 treatment. Blue, vehicle-treated cells. Cells were treated with 0.1 μmol/L VE-822 or vehicle control for 72 hours and apoptosis was quantified as the Annexin-V/PI double-positive population using flow cytometry. Average values of three independent experiments are shown. **E** and **F,** $KPA^{\Delta/\Delta}$ cells display reduced clonogenic after VE-822 treatment, which cannot be observed in *KP*- and $KPA^{fl/\Delta}$ cells. **E,** *KP*-, $KPA^{fl/\Delta}$-, and $KPA^{\Delta/\Delta}$ cell lines were exposed to 0.1 μmol/L VE-822 or vehicle control for 72 hours. Crystal violet stainings were performed after 10 days in culture. **F,** Quantification of crystal violet–positive cells. Scale bar, 500 μm. **G** and **H,** Olaparib treatment induces genotoxic damage, which is not effectively resolved in $KPA^{\Delta/\Delta}$ cells. $KPA^{fl/\Delta}$ cells are partially competent to resolve olaparib-induced genotoxic damage. **G,** *KP*-, $KPA^{fl/\Delta}$-, and $KPA^{\Delta/\Delta}$ cells were either treated with a vehicle control or with olaparib (3 μmol/L, 72 hours). Cells were stained for γH2AX and counterstained with DAPI 3, 24, 48, and 72 hours after treatment initiation. Representative immunofluorescence images are shown. Scale bar, 20 μm. **H,** The percentage of γH2AX-positive cells from the experiment detailed in **G** is quantified. **I** and **J,** VE-822 treatment induces genotoxic damage in *KP*-, $KPA^{fl/\Delta}$-, and $KPA^{\Delta/\Delta}$ cell lines, which cannot be effectively resolved in $KPA^{\Delta/\Delta}$ cells. **I,** *KP*-, $KPA^{fl/\Delta}$-, and $KPA^{\Delta/\Delta}$ cells were either treated with vehicle control or with VE-822 (0.1 μmol/L, 72 hours). Cells were stained for γH2AX and counterstained with DAPI 3, 24, 48, and 72 hours after treatment initiation. Representative immunofluorescence images are shown. Scale bar, 20 μm. **J,** The percentage of γH2AX-positive cells from the experiment detailed in **I** is quantified.

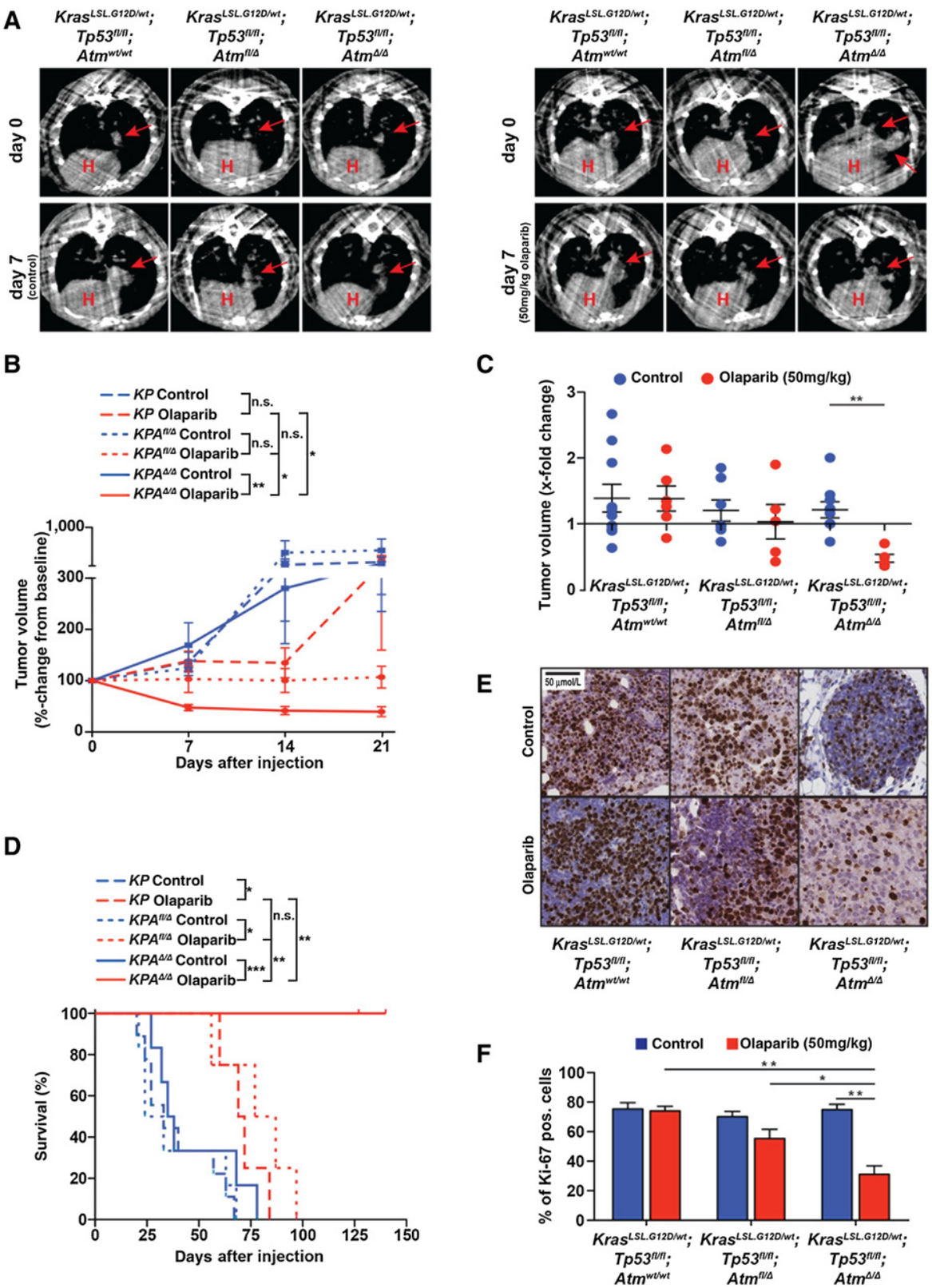

replaced by RAD51 in an ATM/CHK2/BRCA1/BRCA2/PALB2-dependent fashion (15, 36, 37, 39, 40). Rad51 is a critical component of the HR process that mediates homology search, strand exchange, and Holliday junction formation (15). Intriguingly, mutationally encoded defects in the cellular HR machinery are frequently detected in various cancer entities. Particularly, the HR defect in *BRCA1*- or *BRCA2*-deficient settings has previously been shown to be associated with an actionable dependence on PARP1 (24, 25, 41). As ATM is also involved in the HR process and given the PARP1 dependence of *BRCA1*- or *BRCA2*-deficient cells and tumors, we speculated that our *Atm*-deficient *KP* tumors might display an actionable PARP1 dependence. To directly address this question, we assessed the sensitivity of *KP*-, $KPA^{fl/\Delta}$-, and $KPA^{\Delta/\Delta}$ cells against the PARP1 inhibitor olaparib. We initially employed flow cytometry–based apoptosis measurements to directly investigate whether olaparib (3 μmol/L, 120 hours) displayed differential cytotoxicity in *KP*-, $KPA^{fl/\Delta}$-, and $KPA^{\Delta/\Delta}$ cells. As shown in Fig. 5A, olaparib induced only a marginal increase in the fraction of apoptotic *KP* cells, compared with vehicle-treated controls (6.188% ± 0.855% vs. 19.770% ± 3.168%). In contrast, olaparib robustly induced apoptosis in $KPA^{fl/\Delta}$ cells (4.431% ± 0.565% vs. 39.750% ± 4.909%), which was even more pronounced in $KPA^{\Delta/\Delta}$ cells (6.585% ± 0.750% vs. 62.780% ± 7.999; Fig. 5A). We next aimed to validate these observations using clonogenic survival assays. Reminiscent of our flow cytometry results, olaparib induced a mild reduction in surviving *KP* colonies (60.980% ± 3.799%; Fig. 5B and C). The same effect was observed in $KPA^{fl/\Delta}$cells (65.480% ± 2.368%), while $KPA^{\Delta/\Delta}$ cells (11.810% ± 2.288%) showed a striking decrease in surviving colonies (Fig. 5B and C). Thus, our data suggest that heterozygous, and more importantly, homozygous *Atm* deficiency is associated with an actionable PARP1 dependence in *KP* lung adenocarcinoma cell lines.

In addition to profiling the effects of the PARP1 inhibitor olaparib, we next aimed to assess the efficacy of the ATR inhibitor VE-822 (0.1 μmol/L) on *KP*-, $KPA^{fl/\Delta}$-, and $KPA^{\Delta/\Delta}$ cells. These experiments were motivated by recent reports suggesting that ATM depletion or loss might be associated with ATR inhibitor sensitivity in chronic lymphocytic leukemia (42). In addition, the ATR inhibitor AZD6738 was recently shown to potently synergize with cisplatin in *ATM*-deficient non–small cell lung cancer cells (43). Furthermore, combined cisplatin and AZD6738 treatment was shown to induce robust shrinkage of xenograft tumors derived from *KRAS*-mutant and *ATM*-defective human H23 lung adenocarcinoma cells (43). To further interrogate the effects of ATR inhibition on *Atm*-defective lung adenocarcinoma cells, we performed flow cytometry–based apoptosis measurements in *KP*-, $KPA^{fl/\Delta}$-, and $KPA^{\Delta/\Delta}$ cells. As shown in Fig. 5D, VE-822 treatment (0.1 μmol/L, 72 hours) induced only a mild increase in the percentage of apoptotic cells in *KP*- and $KPA^{fl/\Delta}$ cells, compared with vehicle-treated controls (5.548% ± 0.694% vs. 10.170% ± 0.901% and 5.896% ± 0.522% vs. 9.752 ± 0.992%, respectively). In contrast, $KPA^{\Delta/\Delta}$ cells displayed markedly increased levels of apoptosis in response to VE-822 exposure (18.440% ± 1.429%), compared with *KP*- and $KPA^{fl/\Delta}$ cells. Vehicle treatment did not induce substantial levels of apoptosis in $KPA^{\Delta/\Delta}$ cells (5.978% ± 0.776%). These flow cytometry–based apoptosis measurements are further supported by the results of clonogenic survival assays that we performed in *KP*-, $KPA^{fl/\Delta}$-, and $KPA^{\Delta/\Delta}$ cells following ATR inhibition (Fig. 5E and F). Similar to the results shown in Fig. 5D, VE-822 treatment of *KP*- and $KPA^{fl/\Delta}$ cells led to a mild, but statistically significant, reduction in the number of surviving colonies, compared with vehicle-treated cells ($P < 0.0001$ and $P < 0.001$, respectively; Fig. 5E and F). Furthermore, VE-822 exposure led to a substantial and significant reduction in surviving $KPA^{\Delta/\Delta}$ colonies, compared with vehicle controls ($P < 0.0001$; Fig. 5E and F). Of note, the cytotoxic effect of VE-822 was significantly more pronounced in $KPA^{\Delta/\Delta}$ cells, compared with *KP*- and $KPA^{fl/\Delta}$ cells ($P < 0.0001$ and $P < 0.0001$, respectively; Fig. 5D). These differential effects of olaparib (3 μmol/L, 120 hours) and VE-822 (0.1 μmol/L, 72 hours) on *KP*-, $KPA^{fl/\Delta}$-, and $KPA^{\Delta/\Delta}$ cells were also mirrored in longitudinal immunofluorescence-based γH2AX measurements. As shown in Fig. 5G and H and Supplementary Fig. S8A, olaparib induced γH2AX-decorated genotoxic lesions in all three tumor cell genotypes that peaked at 24 hours. While *KP*- and $KPA^{fl/\Delta}$-derived cells displayed substantial clearance of these lesions at 72 hours following drug exposure, $KPA^{\Delta/\Delta}$ cells failed to remove olaparib-induced DNA damage at 72 hours. Similarly, VE-822 was genotoxic in all three genotypes and induced maximal damage at 24 hours following drug exposure (Fig. 5I and J; Supplementary Fig. S8B). These lesions were readily removed by *KP*- and $KPA^{fl/\Delta}$ cells 72 hours following drug exposure. In marked contrast, $KPA^{\Delta/\Delta}$ cells did not display a substantial removal of genotoxic lesions even 72 hours following VE-822 treatment. Thus, in summary, our data indicate that homozygous *Atm* deletion in *KP* murine lung adenocarcinoma cell lines is associated with two distinct molecular vulnerabilities, namely an actionable dependence on PARP1 (Fig. 5A–C, G, and H), as well as an actionable ATR dependence (Fig. 5D–F, I, and J).

Figure 6.

Combined loss of *Atm* and *Tp53* constitutes a genetic constellation that is associated with sensitivity to PARP-inhibition in *Kras*-driven lung adenocarcinomas *in vivo*. **A,** μCT-based response assessment of tumor formation revealed tumor shrinkage in mice bearing $KPA^{\Delta/\Delta}$-derived tumors 7 days following initiation of olaparib treatment (50 mg/kg, i.p., once daily). 10 days after tumor injection, lungs injected with either *KP*-, $KPA^{fl/\Delta}$-, and $KPA^{\Delta/\Delta}$ cells were imaged (μCT) to confirm tumor formation. After 7 days of vehicle (left) or olaparib treatment (right), mice were reimaged. Representative μCT images before (top) and after treatment (bottom) are shown. Red arrows, individual tumor lesions. H, heart. **B** and **C,** Olaparib treatment (50 mg/kg, i.p., once daily) led to a tumor volume reduction in lungs injected with $KPA^{\Delta/\Delta}$ cells. **B,** Tumor volume was longitudinally measured for 21 days. **C,** Tumor volumes were quantified after 7 days of treatment and normalized to pretreatment values (x-fold change, *y*-axis). Volume changes in the treatment cohort (red) were compared with the vehicle-treated control group (blue). Significance is indicated by asterisk and calculated by two-tailed Student *t* test. **D,** Olaparib treatment (50 mg/kg, i.p., once daily) increases overall survival in mice bearing $KPA^{\Delta/\Delta}$-derived tumors, compared with vehicle-treated controls. Mild survival gains were also observed in animals bearing *KP*- and $KPA^{fl/\Delta}$-derived tumors. Survival of animals was followed for 150 days. Survival curves were compared by log-rank (Mantel–Cox) test. **E** and **F,** PARP inhibition induces a significant reduction in Ki-67 positivity in $KPA^{\Delta/\Delta}$-derived tumors, indicating reduced proliferation. **E,** Representative images of Ki-67 stainings. Tumors of all three genotypes (*KP*, $KPA^{fl/\Delta}$, and $KPA^{\Delta/\Delta}$) were treated with vehicle or olaparib for five consecutive days. Scale bar, 50 μm. **F,** Quantification of Ki-67 scores. Significance is indicated by asterisk and calculated by two-tailed Student *t* test. n.s., nonsignificant.

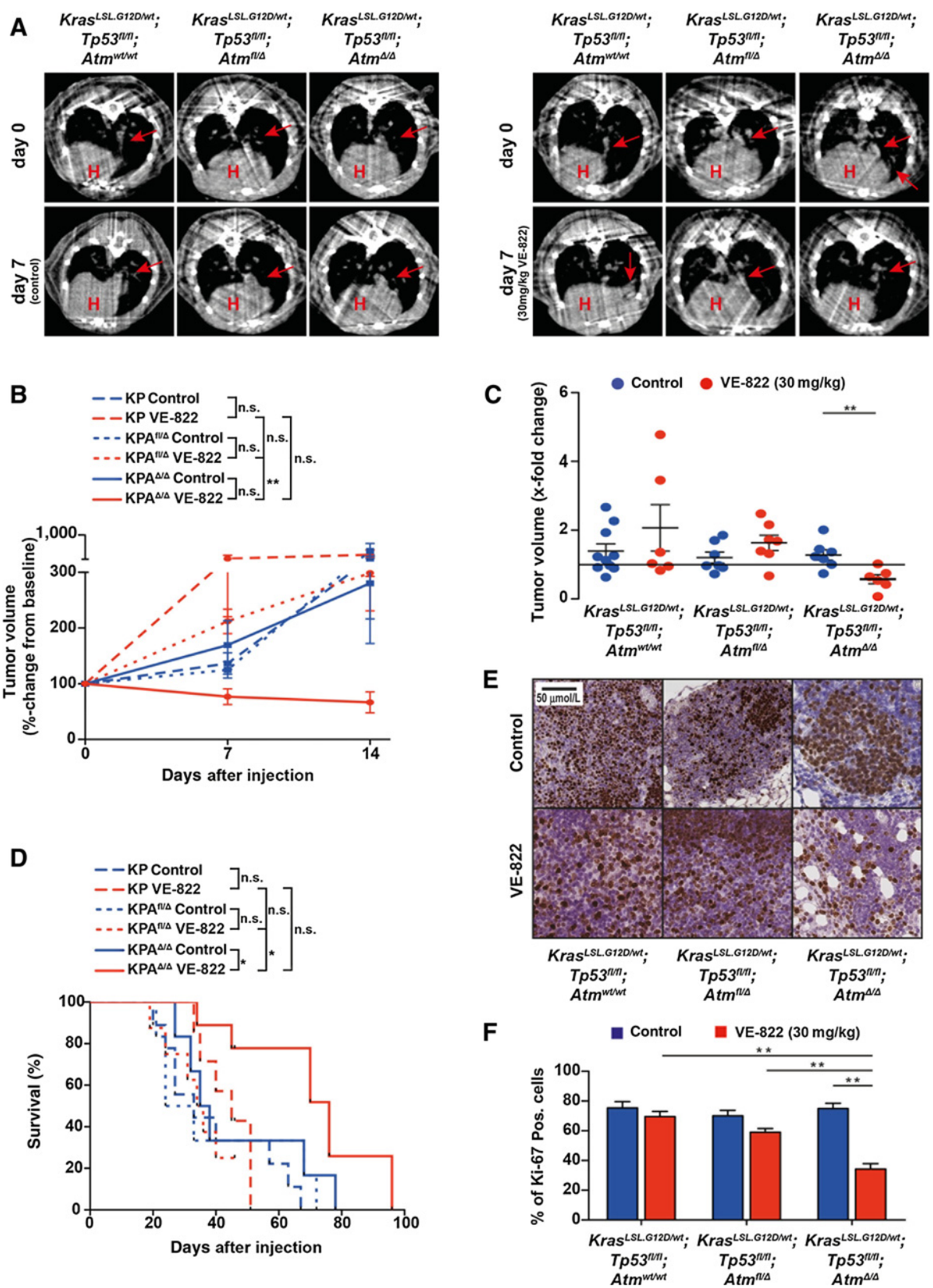

Olaparib and VE-822 display selective toxicity against *Atm*-deficient *Kras$^{G12D/wt}$;Tp53$^{fl/fl}$* lung adenocarcinomas *in vivo*

To solidify our results and to address a potential relevance for human patients, we next asked whether *ATM* is indeed recurrently altered in human lung adenocarcinoma. By reanalyzing human whole-exome sequencing data of 139 lung adenocarcinomas provided by TCGA (44), we found one case that harbored two frameshift deletions in *ATM* (p.R250fs and p.L2006fs). In addition, this sample has undergone a whole-genome duplication and the allelic fractions of both *ATM* mutations clearly indicate that they occurred before the duplication. This suggests that both hits of *ATM* have emerged rather early in the tumor evolution of this patient. These data are further corroborated by recently published observations, which indicate that approximately 40% of human lung adenocarcinomas lack ATM protein expression (7). Mutations are not the only mechanism by which *ATM* expression may be repressed. Epigenetic regulation, as well as posttranscriptional mechanisms may also be involved, suggesting that the fraction of ATM-defective lung adenocarcinoma patients is larger than 1/139 and that both genomic and IHC-based stratification algorithms may be clinically useful.

To further validate our *in vitro* observations, which strongly suggest that *Atm*-deficient *Kras$^{G12D/wt}$;Tp53$^{fl/fl}$* lung adenocarcinoma cells display actionable dependencies on PARP1 and ATR, we next assessed the therapeutic efficacy of single-agent olaparib and VE-822 in our orthotopic transplantation models of *KP*-, *KPA$^{fl/\Delta}$*-, and *KPA$^{\Delta/\Delta}$*-derived tumors (Figs. 6 and 7). While *KP* tumors displayed continued growth (157.5 ± 43.96 percent change in mean tumor volume) in respone to olaparib (50 mg/kg, intraperitoneally, days 1–21), *KPA$^{fl/\Delta}$* tumors remained largely stable in size (107.0 ± 21.09 fold change in mean tumor volume; Fig. 6A–C). In marked contrast, *KPA$^{\Delta/\Delta}$*-derived tumors displayed a robust and statistically significant ($P < 0.001$) volume reduction, which was detectable as early as 7 days following initiation of olaparib treatment (Fig. 6A–C). We note that vehicle-treated *KP*-, *KPA$^{fl/\Delta}$*-, and *KPA$^{\Delta/\Delta}$*-derived tumors displayed continuous growth throughout the entire observation period of 21 days (Fig. 6A–C). In line with these CT-morphologic tumor response data, we observed that olaparib treatment led to a significantly prolonged overall survival in animals bearing *KPA$^{\Delta/\Delta}$*-derived tumors, compared with vehicle-treated controls (36.5 vs. >140.0 days median survival, $P < 0.0001$; Fig. 6D). While olaparib treatment also induced mild survival gains in mice bearing *KP*- and *KPA$^{fl/\Delta}$*-derived tumors (33.0 vs. 70.5 and 28.5 vs. 82.0 days median survival, respectively), this trend was substantially less obvious and the overall survival gains were marginal, compared with the effects observed in *KPA$^{\Delta/\Delta}$* tumor–bearing mice (Fig. 6D). Of note, olaparib treatment (50 mg/kg, intraperitoneally, days 1–21) of *Kras$^{LSL.G12D/wt}$* and *Kras$^{LSL.G12D/wt}$;Atm$^{fl/fl}$* animals bearing autochthonous lung adenocarcinomas revealed similar results (Supplementary Fig. S9A and S9B). While *Kras$^{LSL.G12D/wt}$* tumor–bearing animals did not derive a survival advantage from 21 days of continuous olaparib treatment, *Kras$^{LSL.G12D/wt}$;Atm$^{fl/fl}$* tumor–bearing mice displayed a massive and statistically highly significant survival gain following a 21-day course of intraperitoneal olaparib exposure (Supplementary Fig. S9A and S9B). Together, these data strongly suggest that it is the lack of *Atm*, which dictates the response to olaparib. This synthetic lethal interaction between biallelic *Atm* deletion and PARP1 inhibition appears to be independent of the functional *Tp53* status in *Kras^{G12D}*-driven lung adenocarcinoma.

The cytotoxic effect of olaparib on *KPA$^{\Delta/\Delta}$*-derived tumors was also validated in IHC analyses. We specifically stained *KP*-, *KPA$^{fl/\Delta}$*-, and *KPA$^{\Delta/\Delta}$*-derived tumors with an antibody detecting Ki-67 following *in vivo* olaparib treatment. As shown in Fig. 6E and F and Supplementary Fig. S9, olaparib did not have an effect on the size of the Ki-67–positive tumor cell fraction in *KP*-derived tumors and only induced a mild reduction in Ki-67 positivity in *KPA$^{fl/\Delta}$*-derived tumors. In marked contrast, olaparib treatment led to a massive and statistically highly significant reduction of the Ki-67 index in *KPA$^{\Delta/\Delta}$*-derived tumors. (Fig. 6E and F; Supplementary Fig. S10).

We next aimed to validate the therapeutic efficacy of VE-822 *in vivo*, using our orthotopic transplantation models of *KP*-, *KPA$^{fl/\Delta}$*- and *KPA$^{\Delta/\Delta}$*-derived tumors (Fig. 7). As shown in Fig. 7A–C, VE-822 treatment (30 mg/kg, orally, days 1–3, 8–10, 15–17) of *KP*- and *KPA$^{fl/\Delta}$* tumor–bearing mice did not result in any significant tumor volume changes, compared with vehicle-treated controls. In marked contrast, and in line with our *in vitro* results (Fig. 5D and F), *KPA$^{\Delta/\Delta}$*-derived tumors displayed a substantial and statistically significant volume shrinkage, compared with vehicle-treated controls at day 7 (0.701 ± 0.203 fold change in mean tumor volume, $P = 0.0054$; Fig. 7B and C). This difference was readily detectable on day 7 following initiation of VE-822 treatment and remained detectable throughout the entire observation period of 21 days (Fig. 7B and C). In agreement with these tumor volume assessments, VE-822 treatment also led to a statistically significant ($P < 0.0426$) overall survival extension in *KPA$^{\Delta/\Delta}$* tumor–bearing animals, compared with vehicle-treated controls (36.5 vs. 76 days median survival; Fig. 7D). In contrast, VE-822 did not lead to any significant overall survival gains in mice

Figure 7.

Combined loss of *Atm* and *Tp53* constitutes a genetic constellation that is associated with sensitivity to ATR-inhibition in *Kras*-driven lung adenocarcinomas *in vivo*. **A,** μCT-based response assessment of tumor formation revealed tumor shrinkage in mice bearing *KPA$^{\Delta/\Delta}$*-derived tumors 7 days following initiation of VE-822 treatment (30 mg/kg, orally, days 1–3, 8–10, and 15–17). Ten days after tumor injection, lungs injected with either *KP*-, *KPA$^{fl/\Delta}$*-, and *KPA$^{\Delta/\Delta}$* cells were imaged (μCT) to confirm tumor formation. After 7 days of vehicle (left) or VE-822 treatment (right), mice were reimaged. Representative μCT images before (top) und after treatment (bottom) are shown. Red arrows, individual tumor lesions. H, heart. **B** and **C,** VE-822 treatment (30 mg/kg, orally, days 1–3, 8–10, and 15–17) led to a tumor volume reduction in lungs injected with *KPA$^{\Delta/\Delta}$* cells. **B,** Tumor volume was longitudinally measured for 14 days. **C,** Tumor volumes were quantified after 7 days of treatment and normalized to pretreatment values (x-fold change, *y*-axis). Volume changes in the treatment cohort (red) were compared with vehicle-treated control group (blue). Significance is indicated by asterisk and calculated by two-tailed Student *t* test. **D,** VE-822 treatment (30 mg/kg, orally, days 1–3, 8–10, and 15–17) increases overall survival in mice bearing *KPA$^{\Delta/\Delta}$*-derived tumors, compared with vehicle-treated controls. Survival of animals was followed for 100 days. Survival curves were compared by log-rank (Mantel–Cox) test. **E** and **F,** ATR inhibition induces a significant reduction in Ki-67 scores in mice bearing *KPA$^{\Delta/\Delta}$*-derived tumors, indicating reduced proliferation. **E,** Representative images of Ki-67 stainings. Tumors of all three genotypes (*KP*, *KPA$^{fl/\Delta}$*, and *KPA$^{\Delta/\Delta}$*) were treated with vehicle or VE-822 for three consecutive days. Scale bar, 50 μm. **F,** Quantification of Ki-67 scores. Significance is indicated by asterisk and calculated by two-tailed Student *t* test. n.s., nonsignificant.

bearing *KP*- or $KPA^{fl/\Delta}$-derived tumors (Fig. 7D). These data are further corroborated by IHC experiments. We specifically stained sections of *KP*-, $KPA^{fl/\Delta}$-, and $KPA^{\Delta/\Delta}$-derived tumors following *in vivo* VE-822 treatment with an antibody detecting Ki-67 (Fig. 7E and F; Supplementary Figs. S4 and S10). While VE-822 treatment did not induce a significant reduction in Ki-67 positivity in *KP*- and $KPA^{fl/\Delta}$-derived tumors, this compound induced a significant reduction in Ki-67–positive $KPA^{\Delta/\Delta}$-derived tumors. Altogether, our *in vivo* results clearly demonstrate that the *Atm* status in high-risk *KP* tumors dictates the response to olaparib and VE-822. These data thus imply that the mutational status of *ATM* should be evaluated particularly in high-risk $KRAS^{mut}$ and $TP53^{mut}$ tumors, as biallelic *ATM* alterations predict susceptibility to targeted therapeutic intervention with PARP1 or ATR inhibitors.

Discussion

Lung cancer is the leading cause of cancer-related deaths (1). Through recent cancer genome sequencing efforts, numerous oncogenic driver mutations could be identified in lung adenocarcinoma. Among these are several druggable genomic aberrations, such as oncogenic *EGFR* mutations, as well as *ALK* and *ROS1* rearrangements (4). However, for the majority of lung adenocarcinomas, no direct pharmacologic approach is available to intercept oncogenically rewired signaling. A prominent example for nondruggable oncogenic driver mutations are *KRAS* alterations, which are detected in approximately 32% of human lung adenocarcinomas (5). There is robust experimental evidence indicating that *KRAS*-mutant carcinomas are oncogene addicted (45), which in turn makes *KRAS* an attractive drug target. Recent efforts of suppressing KRAS signaling led to the development of small-molecule inhibitors that bind to the prenyl-binding pocket of PDEδ to prevent the interaction between KRAS and PDEδ (46). Such compounds interfere with oncogenic RAS signaling by altering its intracellular localization and have shown preclinical activity *in vitro* and *in vivo* using xenograft models (46). Currently, the clinical feasibility of such an approach awaits further experimentation. In addition, irreversible allosteric inhibitors of $KRAS^{G12C}$ have recently been developed and were shown to display *in vitro* activity in $KRAS^{G12C}$-mutant cancer cell lines (47). These compounds are thus far limited to the $KRAS^{G12C}$-mutant, as they rely on the mutant cysteine for binding. Hence, direct targeting of *KRAS* remains a difficult challenge and thus far no clinically available KRAS inhibitors have been developed.

As direct targeting of KRAS is difficult, indirect approaches have been proposed. For instance, interception of the downstream effector pathways using combinations consisting of MEK and PI3K inhibitors have been evaluated (48). These regimens have shown promising preclinical activity and multiple clinical trials are underway, but the clinical feasibility and validity has yet to be demonstrated. In addition, combined inhibition of the checkpoint kinases CHK1 and MK2 was recently shown to display preclinical activity against different *Kras*-driven cancer entities (6).

Here, we employed autochthonous mouse models, as well as orthotopic transplantation models of *Kras*-driven standard- and high-risk lung adenocarcinoma to investigate whether cooccurring *Atm* alterations might create a window for therapeutic intervention independent of the driving oncogenic *Kras* p.G12D mutation. While biallelic *Atm* deletions could readily be induced in *Tp53*-proficient *Kras*-driven lung adenocarcinomas (Supplementary Fig. S1), the combined acute Adeno-Cre-induced loss of *Tp53* and *Atm* appeared to be counterselected, *in vivo*. In only 1 of 30 cell lines isolated from primary murine lung adenocarcinoma cell lines isolated from *KPA* mice, could we detect a biallelic loss of *Tp53* and *Atm*. In the remaining 29 cases, we found both alleles of *Tp53* to be effectively recombined, while only one of the *Atm* alleles was deleted. These observations are in line with recently published cancer genome sequencing efforts, which revealed that comutation of *ATM* and *TP53* are significantly underrepresented in lung adenocarcinoma (3, 44, 49). A possible rationale for this observation may be that both genes are involved in the cellular response to genotoxic stress and that combined loss of these central components of the DDR may overwhelm the cellular response mechanisms against DNA damage. Two pieces of circumstantial evidence may support this hypothesis. First, it was recently shown that acute expression of oncogenic *Kras* causes DNA damage, likely due to the induction of replicative stress (6, 50). Second, it was also shown that murine embryonic fibroblasts that were engineered to lack both *Tp53* and *Atm* display a substantially enhanced sensitivity against genotoxic chemotherapeutics, such as the topoisomerase I poisons camptothecin and topotecan, the topoisomerase II poisons doxorubicin, epirubicin and etoposide, as well as the antimetabolites 5-fluorouracil and gemcitabine, but not to cisplatin, carboplatin, and oxaliplatin, and the taxanes, docetaxel and paclitaxel (51). These data are further in line with a previous report, suggesting that combined inactivation of *Tp53* and *Atm* is statistically significantly underrepresented in human tumors (21). Thus, overall, we interpret our observation as follows: the acute combined loss of *Atm* and *Tp53* may be detrimental to the affected cell, due a severely impaired DDR. However, the sequential loss of the two potent tumor suppressor genes may be tolerable, due to the induction of escape mechanisms, such as alternative DNA repair pathways.

Our data clearly indicate that *Kras*-driven murine lung adenocarcinomas that lack *Tp53* and *Atm* are hypersensitive to olaparib, but not cisplatin. This is somewhat surprising, as *BRCA1*- or *BRCA2*-mutant breast cancer patients typically respond very well to cisplatin and olaparib (52). Furthermore, *ATM*, *BRCA1*, and *BRCA2* are all involved in homologous recombination–mediated DNA repair (15). However, in contrast to *ATM*, at least *BRCA2* is also centrally involved in the Fanconi anemia pathway, which is employed to clear interstrand crosslinks—a DNA lesion typically induced by platinum salts (15). Thus, the differential sensitivity of *Atm*-defective lung adenocarcinoma to cisplatin and olaparib may, at least in part, be the result of an impaired HR pathway in these tumor cells. Our data are in line with phenotypes observed in *ATM*-defective DT40 cells, which have been shown to be hypersensitive to PARP inhibition, as well as topoisomerase-I and II poisons (53, 54).

The data presented here clearly indicate that *Kras*-driven lung adenocarcinomas lacking *Atm* develop with similar kinetics as their *Atm*-proficient counterparts in *Tp53* wild-type settings. Furthermore, *Kras*-driven lung adenocarcinomas lacking both *Tp53* and *Atm* do form *in vivo*, albeit at low frequency, thus resembling the human situation. We further demonstrate that biallelic *Atm* deletions are associated with an actionable molecular dependence on PARP1 and ATR activity in both *Tp53*-proficient (standard-risk) and *Tp53*-deficient (high-risk) *Kras*-driven lung adenocarcinomas. Through reanalyzing publicly available exome sequencing data of human lung adenocarcinoma patients, we could demonstrate that tumors with biallelic loss of *ATM* do exist in patients. However, we found only one sample that display

compound heterozygous *ATM* mutations out of 139 tumors that were analyzed. This is somewhat contrasted by recent IHC data indicating that up to 40% of human lung adenocarcinomas display lack of ATM expression. This discrepancy between the different technologies to assess *ATM* status indicates that a clinical patient stratification should probably involve both, sequencing data and IHC. Overall, our observations indicate that genomic aberrations that exist in parallel to the major driving lesions encode therapeutically relevant liabilities. Furthermore, our data implicate that the functional ATM status should be evaluated in human lung adenocarcinomas for which no directly targeted therapeutic approach exists, regardless of the *Tp53* status of these tumors. In fact, our data suggest that the *Atm* deficiency–associated sensitivity against PARP1 and ATR inhibitors is preserved even in *Tp53*-mutant high-risk lung adenocarcinomas.

Disclosure of Potential Conflicts of Interest

M. Peifer is a consultant/advisory board member for NEO New Oncology GmbH. No potential conflicts of interest were disclosed by the other authors.

Authors' Contributions

Conception and design: A. Schmitt, H.C. Reinhardt
Development of methodology: A. Schmitt, D. Welcker
Acquisition of data (provided animals, acquired and managed patients, provided facilities, etc.): A. Schmitt, J. George, M. Nowak, R. Buttner, S. Perner
Analysis and interpretation of data (e.g., statistical analysis, biostatistics, computational analysis): A. Schmitt, G. Knittel, T.-P. Yang, S. Perner, M. Peifer
Writing, review, and/or revision of the manuscript: A. Schmitt, G. Knittel, D. Welcker, R. Buttner, S. Perner, H.C. Reinhardt
Administrative, technical, or material support (i.e., reporting or organizing data, constructing databases): A. Schmitt, J. George, U. Leeser, R. Buttner, H.C. Reinhardt
Study supervision: H.C. Reinhardt

Acknowledgments

We are indebted to our patients, who provided primary material. We thank Alexandra Florin, Marion Müller, and Ursula Rommerscheidt-Fuß from the Institute of Pathology, University Hospital Cologne, for their outstanding technical support. Some analyses conducted in this work were in parts based upon data that was generated by The Cancer Genome Atlas managed by the NCI and NHGRI.

Grant Support

This work was supported by the Volkswagenstiftung (Lichtenberg Program; H.C. Reinhardt), the Deutsche Forschungsgemeinschaft (KFO-286; H. C. Reinhardt and M. Peifer), the Bundesministerium für Bildung und Forschung (SMOOSE; H. C. Reinhardt, M. Peifer, R. Büttner and MILES, M. Peifer), the German federal state North Rhine Westphalia (NRW) as part of the EFRE initiative (grant LS-1-1-030a to H. C. Reinhardt), the Else Kröner-Fresenius Stiftung (EKFS-2014-A06 to H. C. Reinhardt), and the Deutsche Krebshilfe (111724 to H. C. Reinhardt).

The costs of publication of this article were defrayed in part by the payment of page charges. This article must therefore be hereby marked *advertisement* in accordance with 18 U.S.C. Section 1734 solely to indicate this fact.

Received December 20, 2016; revised March 9, 2017; accepted March 27, 2017; published OnlineFirst March 31, 2017.

References

1. Jemal A, Bray F, Center MM, Ferlay J, Ward E, Forman D. Global cancer statistics. CA Cancer J Clin 2011;61:69–90.
2. Torre LA, Bray F, Siegel RL, Ferlay J, Lortet-Tieulent J, Jemal A. Global cancer statistics, 2012. CA Cancer J Clin 2015;65:87–108.
3. Ding L, Getz G, Wheeler DA, Mardis ER, McLellan MD, Cibulskis K, et al. Somatic mutations affect key pathways in lung adenocarcinoma. Nature 2008;455:1069–75.
4. Novello S, Barlesi F, Califano R, Cufer T, Ekman S, Levra MG, et al. Metastatic non-small-cell lung cancer: ESMO Clinical Practice Guidelines for diagnosis, treatment and follow-up. Ann Oncol 2016;27: v1–v27.
5. Clinical Lung Cancer Genome Project, Network Genomic Medicine. A genomics-based classification of human lung tumors. Sci Transl Med 2013;5:209ra153.
6. Dietlein F, Kalb B, Jokic M, Noll EM, Strong A, Tharun L, et al. A synergistic interaction between Chk1- and MK2 inhibitors in KRAS-mutant cancer. Cell 2015;162:146–59.
7. Villaruz LC, Jones H, Dacic S, Abberbock S, Kurland BF, Stabile LP, et al. ATM protein is deficient in over 40% of lung adenocarcinomas. Oncotarget 2016;7:57714–25.
8. Reinhardt HC, Yaffe MB. Phospho-Ser/Thr-binding domains: navigating the cell cycle and DNA damage response. Nat Rev Mol Cell Biol 2013;14:563–80.
9. Morandell S, Reinhardt HC, Cannell IG, Kim JS, Ruf DM, Mitra T, et al. A reversible gene-targeting strategy identifies synthetic lethal interactions between MK2 and p53 in the DNA damage response in vivo. Cell Rep 2013;5:868–77.
10. Reinhardt HC, Aslanian AS, Lees JA, Yaffe MB. p53-deficient cells rely on ATM- and ATR-mediated checkpoint signaling through the p38MAPK/MK2 pathway for survival after DNA damage. Cancer Cell 2007;11: 175–89.
11. Reinhardt HC, Hasskamp P, Schmedding I, Morandell S, van Vugt MA, Wang X, et al. DNA damage activates a spatially distinct late cytoplasmic cell-cycle checkpoint network controlled by MK2-mediated RNA stabilization. Mol Cell 2010;40:34–49.
12. Bulavin DV, Higashimoto Y, Popoff IJ, Gaarde WA, Basrur V, Potapova O, et al. Initiation of a G2/M checkpoint after ultraviolet radiation requires p38 kinase. Nature 2001;411:102–7.
13. Shiloh Y. ATM and related protein kinases: safeguarding genome integrity. Nat Rev Cancer 2003;3:155–68.
14. Shiloh Y, Ziv Y. The ATM protein kinase: regulating the cellular response to genotoxic stress, and more. Nat Rev Mol Cell Biol 2013; 14:197–210.
15. Dietlein F, Thelen L, Reinhardt HC. Cancer-specific defects in DNA repair pathways as targets for personalized therapeutic approaches. Trends Genet 2014;30:326–39.
16. Ripolles L, Ortega M, Ortuno F, Gonzalez A, Losada J, Ojanguren J, et al. Genetic abnormalities and clinical outcome in chronic lymphocytic leukemia. Cancer Genet Cytogenet 2006;171:57–64.
17. Haidar MA, Kantarjian H, Manshouri T, Chang CY, O'Brien S, Freireich E, et al. ATM gene deletion in patients with adult acute lymphoblastic leukemia. Cancer 2000;88:1057–62.
18. Knittel G, Liedgens P, Reinhardt HC. Targeting ATM-deficient CLL through interference with DNA repair pathways. Front Genet 2015;6:207.
19. Waddell N, Pajic M, Patch A-M, Chang DK, Kassahn KS, Bailey P, et al. Whole genomes redefine the mutational landscape of pancreatic cancer. Nature 2015;518:495–501.
20. Austen B, Skowronska A, Baker C, Powell JE, Gardiner A, Oscier D, et al. Mutation status of the residual ATM allele is an important determinant of the cellular response to chemotherapy and survival in patients with chronic lymphocytic leukemia containing an 11q deletion. J Clin Oncol 2007;25:5448–57.
21. Jiang H, Reinhardt HC, Bartkova J, Tommiska J, Blomqvist C, Nevanlinna H, et al. The combined status of ATM and p53 link tumor development with therapeutic response. Genes Dev 2009;23: 1895–909.

22. Goodarzi AA, Noon AT, Deckbar D, Ziv Y, Shiloh Y, Lobrich M, et al. ATM signaling facilitates repair of DNA double-strand breaks associated with heterochromatin. Mol Cell 2008;31:167–77.
23. Jeggo PA, Geuting V, Lobrich M. The role of homologous recombination in radiation-induced double-strand break repair. Radiother Oncol 2011; 101:7–12.
24. Bryant HE, Schultz N, Thomas HD, Parker KM, Flower D, Lopez E, et al. Specific killing of BRCA2-deficient tumours with inhibitors of poly(ADP-ribose) polymerase. Nature 2005;434:913–7.
25. Farmer H, McCabe N, Lord CJ, Tutt AN, Johnson DA, Richardson TB, et al. Targeting the DNA repair defect in BRCA mutant cells as a therapeutic strategy. Nature 2005;434:917–21.
26. Middleton FK, Patterson MJ, Elstob CJ, Fordham S, Herriott A, Wade MA, et al. Common cancer-associated imbalances in the DNA damage response confer sensitivity to single agent ATR inhibition. Oncotarget 2015;6: 32396–409.
27. Krajewska M, Fehrmann RS, Schoonen PM, Labib S, de Vries EG, Franke L, et al. ATR inhibition preferentially targets homologous recombination-deficient tumor cells. Oncogene 2015;34:3474–81.
28. DuPage M, Dooley AL, Jacks T. Conditional mouse lung cancer models using adenoviral or lentiviral delivery of Cre recombinase. Nat Protoc 2009;4:1064–72.
29. Zha S, Sekiguchi J, Brush JW, Bassing CH, Alt FW. Complementary functions of ATM and H2AX in development and suppression of genomic instability. Proc Natl Acad Sci U S A 2008;105:9302–6.
30. Jokic M, Vlasic I, Rinneburger M, Klumper N, Spiro J, Vogel W, et al. Ercc1 deficiency promotes tumorigenesis and increases cisplatin sensitivity in a TP53 context-specific manner. Mol Cancer Res 2016;14: 1110–23.
31. Jonkers J, Meuwissen R, van der Gulden H, Peterse H, van der Valk M, Berns A. Synergistic tumor suppressor activity of BRCA2 and p53 in a conditional mouse model for breast cancer. Nat Genet 2001;29:418–25.
32. Xu Y, Ashley T, Brainerd EE, Bronson RT, Meyn MS, Baltimore D. Targeted disruption of ATM leads to growth retardation, chromosomal fragmentation during meiosis, immune defects, and thymic lymphoma. Genes Dev 1996;10:2411–22.
33. Hoeijmakers JH. Genome maintenance mechanisms for preventing cancer. Nature 2001;411:366–74.
34. Lees-Miller SP, Meek K. Repair of DNA double strand breaks by non-homologous end joining. Biochimie 2003;85:1161–73.
35. Lieber MR. The mechanism of double-strand DNA break repair by the nonhomologous DNA end-joining pathway. Annu Rev Biochem 2010;79: 181–211.
36. Heyer WD, Ehmsen KT, Liu J. Regulation of homologous recombination in eukaryotes. Annu Rev Genet 2010;44:113–39.
37. Krejci L, Altmannova V, Spirek M, Zhao X. Homologous recombination and its regulation. Nucleic Acids Res 2012;40:5795–818.
38. Morrison C, Sonoda E, Takao N, Shinohara A, Yamamoto K, Takeda S. The controlling role of ATM in homologous recombinational repair of DNA damage. EMBO J 2000;19:463–71.
39. Sung P, Klein H. Mechanism of homologous recombination: mediators and helicases take on regulatory functions. Nat Rev Mol Cell Biol 2006;7:739–50.
40. San Filippo J, Sung P, Klein H. Mechanism of eukaryotic homologous recombination. Annu Rev Biochem 2008;77:229–57.
41. Tutt A, Robson M, Garber JE, Domchek SM, Audeh MW, Weitzel JN, et al. Oral poly(ADP-ribose) polymerase inhibitor olaparib in patients with BRCA1 or BRCA2 mutations and advanced breast cancer: a proof-of-concept trial. Lancet 2010;376:235–44.
42. Kwok M, Davies N, Agathanggelou A, Smith E, Petermann E, Yates E, et al. Synthetic lethality in chronic lymphocytic leukaemia with DNA damage response defects by targeting the ATR pathway. Lancet 2015;385Suppl 1: S58.
43. Vendetti FP, Lau A, Schamus S, Conrads TP, O'Connor MJ, Bakkenist CJ. The orally active and bioavailable ATR kinase inhibitor AZD6738 potentiates the anti-tumor effects of cisplatin to resolve ATM-deficient non-small cell lung cancer in vivo. Oncotarget 2015;6:44289–305.
44. The Cancer Genome Atlas Research Network. Comprehensive molecular profiling of lung adenocarcinoma. Nature 2014;511:543–50.
45. Fisher GH, Wellen SL, Klimstra D, Lenczowski JM, Tichelaar JW, Lizak MJ, et al. Induction and apoptotic regression of lung adenocarcinomas by regulation of a K-Ras transgene in the presence and absence of tumor suppressor genes. Genes Dev 2001;15:3249–62.
46. Zimmermann G, Papke B, Ismail S, Vartak N, Chandra A, Hoffmann M, et al. Small molecule inhibition of the KRAS-PDEdelta interaction impairs oncogenic KRAS signalling. Nature 2013;497:638–42.
47. Ostrem JM, Peters U, Sos ML, Wells JA, Shokat KM. K-Ras(G12C) inhibitors allosterically control GTP affinity and effector interactions. Nature 2013; 503:548–51.
48. Engelman JA, Chen L, Tan X, Crosby K, Guimaraes AR, Upadhyay R, et al. Effective use of PI3K and MEK inhibitors to treat mutant Kras G12D and PIK3CA H1047R murine lung cancers. Nat Med 2008;14:1351–6.
49. Campbell JD, Alexandrov A, Kim J, Wala J, Berger AH, Pedamallu CS, et al. Distinct patterns of somatic genome alterations in lung adenocarcinomas and squamous cell carcinomas. Nat Genet 2016;48:607–16.
50. Di Micco R, Fumagalli M, Cicalese A, Piccinin S, Gasparini P, Luise C, et al. Oncogene-induced senescence is a DNA damage response triggered by DNA hyper-replication. Nature 2006;444:638–42.
51. Fedier A, Schlamminger M, Schwarz VA, Haller U, Howell SB, Fink D. Loss of atm sensitises p53-deficient cells to topoisomerase poisons and anti-metabolites. Ann Oncol 2003;14:938–45.
52. Turner NC, Tutt AN. Platinum chemotherapy for BRCA1-related breast cancer: do we need more evidence? Breast Cancer Res 2012;14:115.
53. Maede Y, Shimizu H, Fukushima T, Kogame T, Nakamura T, Miki T, et al. Differential and common DNA repair pathways for topoisomerase I- and II-targeted drugs in a genetic DT40 repair cell screen panel. Mol Cancer Ther 2014;13:214–20.
54. Murai J, Huang SY, Das BB, Renaud A, Zhang Y, Doroshow JH, et al. Trapping of PARP1 and PARP2 by clinical PARP inhibitors. Cancer Res 2012;72:5588–99.